

國立交通大學
光電工程研究所

碩士論文

半極化面{10-11}氮化銦鎵/氮化鎵奈米金字塔

發光二極體之製作及特性研究

Fabrication and investigation of semipolar {10-11}
InGaN/GaN nanopyramid light emitting diode

研究生：陳羿蓁

指導教授：郭浩中 教授

鄒志偉 教授

中華民國一〇一〇年七月

國立交通大學
光電工程研究所

碩士論文

半極化面{10-11}氮化銦鎵/氮化鎵奈米金字塔

發光二極體之製作及特性研究

Fabrication and investigation of semipolar {10-11}
InGaN/GaN nanopyramid light emitting diode

研究生：陳羿蓁

指導教授：郭浩中 教授

鄒志偉 教授

中華民國一百年七月

半極化面{10-11}氮化銦鎵/氮化鎵奈米金字塔發光二極體之
製作及特性研究

Fabrication and investigation of semipolar {10-11} InGaN/GaN
nanopyramid light emitting diode

研究生：陳羿蓁

Student：Yi-Chen Chen

指導教授：郭浩中 教授

Advisor：Hao-Chung Kuo

鄒志偉 教授

Chi-Wai Chow

國立交通大學

光電工程研究所

碩士論文

A Thesis

Submitted to Institute of Electro-Optical Engineering

College of Electrical Engineering

National Chiao Tung University

in Partial Fulfillment of the Requirements

for the Degree of

Master

In

Electro-Optical Engineering

July 2011

Hsinchu, Taiwan, Republic of China

中華民國一百年七月

半極化面{10-11}氮化鎵鎵/氮化鎵奈米金字塔發光二極體之

製作及特性研究

研究生：陳羿蓁

指導教授：郭浩中 教授

鄒志偉 教授

國立交通大學光電工程研究所

摘要

在本論文中，我們介紹高性能綠光發光二極體用選區成長技術將半極化面{10-11}氮化鎵奈米金字塔成長於藍寶石基板上。

從穿透式電子顯微鏡(transmission electron microscopy, TEM)影像中發現選區成長技術可以減少半極化面{10-11}多重量子阱內的穿透錯位密度。而且，從變功率光激發螢光(Photoluminescence, PL)量測可以看出半極化面多重量子阱的內建電場較小、內部量子效率較高。另外，時間解析光激發螢光(Time resolved Photoluminescence, TRPL)量測顯示半極化面{10-11}多重量子阱的輻射複合時間遠小於極化面(0001)多重量子阱。這些分析結果可以歸納出因為使用半極化面{10-11}多重量子阱而確實能夠減緩量子阱中的量子侷限史塔克效應(Quantum confined Stark effect, QCSE)。

最後，我們將做成元件的綠光、黃綠光、橘光發光二極體用電激發螢光(Electroluminescence, EL)量測分析出 I - V 曲線。此外，我們用空間解析陰極射線激發螢光(Cathodoluminescence, CL)量測做變電流大小電激發螢光(Electroluminescence, EL)量測的光譜分析討論。

Fabrication and investigation of semipolar {10-11} InGaN/GaN nanopyramid light emitting diode

Student : Yi-Chen Chen

Advisor : Hao-Chung Kuo

Chi-Wai Chow

Institute of Electro-Optical Engineering

National Chiao Tung University

Abstract

In this study, we presented high performance green emission semipolar {10-11} GaN-based nanopyramid light emitting diodes (LEDs) grown on c-plane sapphire substrate by selective area epitaxy (SAE).

The transmission electron microscopy (TEM) images suggest that the SAE can suppress the threading dislocation density in the semipolar {10-11} multiple quantum well (MQWs). Besides, from power dependent PL measurement, the internal electric field (IEF) of semipolar MQWs was reduced, and the internal quantum efficiency (IQE) was improved. Moreover, time-resolved PL (TRPL) measurement shows the radiative recombination lifetime of semipolar MQWs was shorter than that of c-plane MQWs. These results could strongly confirm the reduction of quantum confined Stark effect (QCSE) by using semipolar MQWs.

Finally, the $L-I-V$ curves of green, olivine and orange emission nanopyramid LEDs were investigated by electroluminescence (EL) measurement. And the EL peak shift and emission behavior could be referred to the spatial distribution of nanopyramid, which was investigated by cathodoluminescence (CL) measurement.

Acknowledgements

時間流逝得很快，轉眼間兩年的碩士生涯就要結束了，在研究論文的過程中受到了太多人太多的幫助了，如果少了你們的幫忙，就不會成就現在的我。

首先，誠摯的感謝指導教授郭浩中老師、鄒志偉老師和中研院的程育人老師，在研究的過程中總是不厭其煩的與我討論，給了我許多有用的意見還有鼓勵，另外，感謝老師提供良好的實驗儀器設備，使我的研究可以進行得很順利。

感謝 Epi team 大家長李博，在咪聽的過程中教導了我們非常多的專業知識；感謝金釵，在我有疑惑的時候總是耐心的幫我解答；感謝鏡學，不論多基礎的問題都願意回答我；感謝 DAVID，做實驗的時候常常及時救援；感謝宅宅 Jo 博，願意犧牲自己的休閒時間幫我改英文；感謝專業的藍博，對於實驗儀器一把罩；感謝阿伯，CL 不知道幫我打了多少次；感謝 PM 博明學長，很認真的跟我們討論遇到的問題；感謝聰明的哲榮，可以很快的找出問題點並提供解決的辦法；最最感謝詹姆世邦，這一年多來我真的學習到了很多，謝謝你給我這麼好的題目，讓我的碩班研究之路非常充實。感謝所有幫助過我的學長姊，不論是言語上的鼓勵或者是疑難雜症的解惑都讓我學到了很多。

感謝誠實的瑋婷，不經意的話都很有爆點，什麼心事都可以互相分享，謝謝你回答了我很多關於 EL 的問題；感謝慢一拍 kaka，卡式風格讓我笑到肚子長肌肉，超級好揪的跟團咖；感謝季瑾，大老遠的跑過來跟我們咪聽；感謝厲害的昀瑾，SketchUp 大神，為難你忙碩論還要幫我趕圖；感謝少根筋 90，雖然講話超誇張但我還是很愛聽，出去玩都麻煩你規劃路線，謝謝你充電之旅幫我那麼多的忙；感謝正義魔人肉圓，剛到新竹人生地不熟的時候給我很多幫助，一開始的

美食團也都仰仗你，謝謝你開心的接受你的外號；感謝攝影大師幼齒，每次出去都背著很重的傢伙，有的沒的都可以亂說，謝謝你聽了我那麼多抱怨；感謝小朋友的家齊，總是很準時抵達大家約定的地點，下次會好好保護你的，謝謝你幫我分擔了很多 PL 的實驗；感謝愛妻小杜，大量買東西都要靠你的車，謝謝你在製程上幫了我很多的忙；感謝大神阿 po，就算沒搞清楚狀況還是會跟團，不論如何都會排除萬難的出現；感謝幽默的大寶，讓人無法忘記的飄逸背影，勞煩你每次照完都還會幫大家刪除醜照；感謝優秀的阿國，很阿莎力的把禮物服裝表演一番，沒有服裝的表演也讓大家很開心；感謝股票專家冠霖，提供了很多公司的情報，以後變成專家別忘了幫我理財；感謝帥氣的 Just，蜂蜜牛奶超好喝的，每次聽到讚美心情都很好；感謝美食專家 SGG，很多餐廳的資訊都知道，每次需要換錢都很方便；感謝訓利哥，工數超級厲害，謝謝你代替大家獻花；感謝所有碩二，謝謝大家陪我一起瘋瘋狂狂瘋瘋癲癲的四處闖蕩，讓我的碩班生涯多采多姿，留下了非常多美好的回憶，不論何時只要想到你們都會很開心，真的很高興能夠遇到你們，我們一定要成為永遠的朋友！

感謝超級威 Ben Sou，幫我分擔很多煩惱，不論任何軟體、實驗、模擬都難不倒，謝謝你願意花那麼多的時間幫助我；感謝 pink 雨婷、球男哲宇，幫忙分擔了很多量測實驗；感謝乖巧 Bush，常常麻煩你做 EL，你也都很願意幫忙；感謝魔王，幫我做了很多製程；感謝老漢，幫我量積分球；感謝所有碩一，共同擁有了很多在實驗室的回憶。

最後，要感謝我最親愛的家人，謝謝你們總是支持我做的決定，常常關心和鼓勵我，讓我可以很順利的念到碩士畢業，我會永遠好愛好愛你們！

Content

摘要.....	i
Abstract.....	ii
Acknowledgements.....	iii
Content.....	iv
List of Tables.....	vi
List of Figures.....	vii

Chapter 1 Introduction

1.1 Development of III-Nitride Light-Emitting Diodes	
1.1.1 Wide bandgap III-nitride Materials.....	1
1.1.2 History of GaN-based LEDs.....	2
1.2 Nonpolar and Semipolar III-Nitride Light-Emitting Diodes: Achievements and Challenges.....	4
1.3 Motivation.....	8

Chapter 2 Experimental Instruments and Methods

2.1 Transmission electron microscope (TEM)	11
2.2 Photoluminescence spectroscopy (PL)	
2.2.1 Power dependent and temperature dependent PL.....	15
2.2.2 Time-resolved PL (TRPL)	17
2.3 Electroluminescence spectroscopy (EL)	20
2.4 Scanning electron microscope-Cathodoluminescence (SEM-CL).....	22

Chapter 3 Sample structure and fabrication

3.1 Fabrication of GaN nanopyramids with semipolar {10-11} InGaN/GaN MQWs.....	24
--	----

3.2	Crystal quality analysis of the semipolar {10-11} InGaN/GaN multiple quantum wells (MQWs)	28
3.3	Spatial resolved cathodoluminescence (CL) of nanopyramid structure.....	31

Chapter 4 Optical Analysis of Polar and Semipolar MQWs

4.1	Investigation of internal electron field (IEF)	
4.1.1	Introduction.....	34
4.1.2	Calculation.....	35
4.1.3	Experimental result and discussion.....	40
4.2	Property of the internal quantum efficiency (IQE)	
4.2.1	Theory and measurement of IQE.....	42
4.2.2	Experimental result and discussion.....	44
4.3	Carrier dynamic of multiple quantum wells (MQWs)	
4.3.1	Analysis of carrier lifetime.....	47
4.3.2	Experimental result and discussion.....	49

Chapter 5 Electrical Property of III-nitride LED

5.1	Device performance of green nanopyramid LED.....	52
5.2	Device performance of olivine nanopyramid LED.....	59
5.3	Device performance of orange nanopyramid LED.....	62

Chapter 6 Conclusion.....66

Reference.....	68
-----------------------	-----------

List of Tables

Table 1.2-1	The efficiency of 12 mil standard red, green and Blue LED at injected current 20 mA with carrier density about $2 \times 10^{17} \text{ cm}^{-3}$6
Table 4.3-1	The calculation result of τ_r and τ_{nr} from TRPL measurement.....50



List of Figures

Figure 1.1-1	Bandgap energy versus lattice constant of III-V nitride semiconductors at room temperature.....	1
Figure 1.1-2	The schematic drawing of InGaN LED.....	4
Figure 1.2-1	Figure 1.2-1 The external quantum efficiency (EQE) bench mark of III-V semiconductor among visible light region.....	5
Figure 1.2-2	The QW structures on (a) polar and (b) nonpolar orientations and their band diagrams.....	7
Figure 1.2-3	The polarization charge density as a function of tilt angle of the growth plane with respect to the c-plane in different In composition InGaN QWs.....	8
Figure 2.1-1	Ray diagram showing two basic operations of TEM.....	12
Figure 2.2-1	Interband transitions in photoluminescence system.....	13
Figure 2.2-2	The schematic of PL measurement system.....	16
Figure 2.2-3	The picture of PL measurement system.....	17
Figure 2.2-4	Detector signal for fluorescence detection at a pulse repetition rate of 80 MHz.....	18
Figure 2.2-5	Principle of TCSPC.....	19
Figure 2.3-1	The schematic of EL measurement system.....	21
Figure 2.3-2	The picture of EL measurement system.....	22
Figure 2.4-1	Schematic diagram of a scanning electron microscope.....	23
Figure 3.1-1	The flow chart of nano imprint lithography (NIL).....	25
Figure 3.1-2	Illustrations of fabrication process of nanopyramid MQWs. (a) GaN template contained 1 μm undoped GaN and 1 μm n-type GaN. (b) A 400 nm SiO ₂ layer and a 200 nm polymer layer were deposited. (c) Nanorod patterns were formed by nano imprint lithography (NIL) technique. (d) Passivated with porous SiO ₂ at sidewall. (e) Schematic structure of GaN-based nanorod structure with the regrowth of semipolar {10-11} GaN pyramids and 10-pair In _{0.3} Ga _{0.7} N/GaN (3nm/12nm) MQWs.....	26

Figure 3.1-3	The angle-view SEM images of (a) GaN nanorod arrays. (b) GaN nanorod with sidewall passivation. (c) GaN nanoarrow arrays with semipolar {10-11} In _{0.3} Ga _{0.7} N/GaN MQW.....	27
Figure 3.1-4	Illustration of nanopyramid LED device.....	28
Figure 3.2-1	The TEM images of (a) GaN nanorod with semipolar nanopyramids. (b) Enlarge view of semipolar {10-11} MQWs.....	29
Figure 3.2-2	The mechanism of reduce threading dislocation density(TDD) in semipolar {10-11} MQWs by (a) nano imprint lithography (NIL) and (b) epitaxy lateral overgrowth (ELO).....	30
Figure 3.3-1	Top view CL spectrum of semipolar MQWs.....	32
Figure 3.3-2	(a) Top view SEM image. CL emission signal at fix emission wavelength (b) 460 nm, (c) 480 nm, (d) 500 nm, (e) 520 nm, (f) 540 nm, (g) 560 nm and (h) 580 nm, respectively.....	33
Figure 4.1-1	(a) Energy band diagram of a p-n junction under exciting light. (b) Idealized equivalent circuit.....	36
Figure 4.1-2	The infinite quantum well.....	38
Figure 4.1-3	The PL peak emission energy with different excitation power for the semipolar and c-plane MQWs (symbols) at T=15 K. The solid lines are the internal electron field (IEF) fitting results from Equation (4.1-13).....	41
Figure 4.2-1	Internal quantum efficiency (IQE) as a function of different injected carrier density for semipolar MQWs.....	45
Figure 4.2-2	Internal quantum efficiency (IQE) as a function of different injected carrier density for c-plane MQWs.....	45
Figure 4.2-3	The simulated energy band diagram from the internal electron field fitting results of (a) c-plane and (b) semipolar QW, respectively.....	46
Figure 4.3-1	Illustration of radiative and nonradiative transition in a semiconductor.....	48
Figure 4.3-2	The TRPL spectrum of c-plane and semipolar MQWs at low temperature (LT) and room temperature (RT).....	50

Figure 5.1-1	(Color online) The light output power density (mW/cm^2) versus forward current and current versus voltage of nanopyr amid LED. Background: A photograph image taken under an injection current of 50 mA.....	53
Figure 5.1-2	(a) The EL emission spectrum with different injected current at room temperature. (b) The two peaks wavelength shift from EL spectrum.....	54
Figure 5.1-3	The photograph images taken under injection current of (a) 10 mA, (b) 30 mA and (c) 100 mA.....	56
Figure 5.1-4	The EL spectrum under forward current of 10 mA, 30 mA and 100 mA, respectively (solid line). The results of Gauss multiple peaks fitting (Dash line).....	57
Figure 5.1-5	The schematic diagram of nanopyr amid LED under (a) very low and (b) high injected current.....	58
Figure 5.2-1	(Color online) The light output power density (mW/cm^2) and forward voltage versus forward current of nanopyr amid LED. Background: An electrical luminescence image taken under injection current 50 mA.....	60
Figure 5.2-2	(a) The EL emission spectrum with different injected current at room temperature. (b) The two peaks wavelength shift from EL spectrum.....	61
Figure 5.3-1	(Color online) The light output power density (mW/cm^2) versus forward current and current versus voltage of nanopyr amid LED. Background: A photograph image taken under an injection current of 200 mA.....	62
Figure 5.3-2	(a) The EL emission spectrum with different injected current at room temperature. (b) The two peaks wavelength shift from EL spectrum.....	64

Chapter 1. Introduction

1.1 Development Characteristic of III-Nitride Light-Emitting Diodes

1.1.1 Wide bandgap III-nitride Materials

The III-nitride materials have attracted much attention due to its tremendous potential for fabricating light emitting diodes (LEDs) with a full color application. The bandgap of the wurtzite polytypes of III-nitrides material cover a very wide range, from 0.7 eV for InN to 6.1 eV for AlN, which represents the emission wavelength from infrared (IR) region to deep ultraviolet (UV). **Figure 1.1-1** shows the bandgaps of various alloys of III-Nitrides [1].

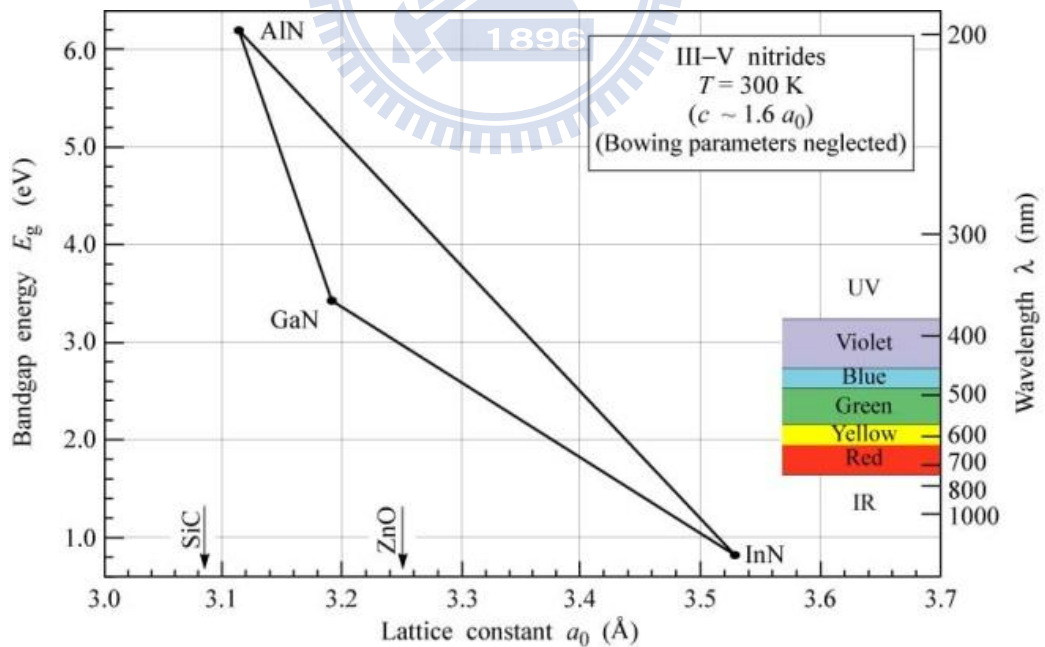


Figure 1.1-1 Bandgap energy versus lattice constant of III-V nitride semiconductors at room temperature.

With such wide emission wavelength range, III-nitrides materials is promising for applying in the applications of optoelectronic devices such as flat panel display, competing storage technologies, automobiles, general lighting and biotechnology, and so on [2-4].

With some unique properties, the III-nitride semiconductor material is not only suitable for lighting source in short wavelength in visible region but also high-speed/high-power electron device [5]. For instance, it has high bond energy (~ 2.3 eV), high-saturation velocity ($\sim 2.7 \times 10^4$ cm/s), high-breakdown field ($\sim 2 \times 10^6$ V/cm), and strong excitonic effects (> 50 meV) [6-7].

Although III-nitride semiconductors are suitable for applying in high efficiency lighting devices, they also have some inherent drawbacks to deteriorate the lighting efficiency like internal piezoelectric field and spontaneous polarization at heterointerface leading to the quantum confined Stark effect (QCSE) and causing charge separation between electrons and holes in quantum wells [8-9]. Even though, it is still worth to devote more effort to overcome such problems for its great potential in solid state lighting and some groups had indeed succeeded in solving parts of this problems.

1.1.2 History of GaN-based LEDs

Light Emitting Diodes (LEDs) are solid state devices which emit light when electrical current passes through them. In LEDs made of semiconductors, the color of

the light depends on the bandgap of the semiconductor material, proceeding from red through orange, yellow, green, blue and violet as the gap increases.

The first blue light-emitting diode (LED) using III-Nitrides materials was fabricated by J. I. Pankove et al. [10] with an metal-i-n structure in 1972. Since that, related research is going on continually. However, progresses have been limited because of highly background n-type concentration resulting from the native defects commonly thought to be nitrogen vacancies and residual impurities such as Si and oxygen acted as an efficient donor, poorly conducting p-type GaN, and the lack of appropriate substrates for epitaxial growth. Until late 1980s, H. Amano et al. [11, 12] discovered a very useful application of a low-temperature buffer layer and developed low-energy electron beam interaction (LEEBI) techniques to obtain better GaN epilayer and conductive p-type GaN, initiated a new strong interest in this research field. Finally, the first GaN-based blue LED constructed of a real p-n junction was achieved, which had greatly improved in the device performance. However, the acceptor concentration of p-type GaN is still too low such that the application of these materials is still unreliable. After that, in 1992, S. Nakamura et al. [13] achieved better conductive p-type GaN material by introducing a simple thermal annealing procedure in nitrogen ambient (≥ 750 °C). Afterward Nakamura and Mukai [14] succeeded in growing high-quality InGaN films that emitted strong band-to-band emission from green to UV by changing the indium content of InGaN with a two-flow MOCVD method. Nowadays, Most of III-Nitride based light emitting devices uses InGaN as

active layer instead of GaN because the difficulty of fabricating high efficiency GaN based light emitting devices. Adding a small amount of indium into the GaN is very important to obtain a strong band-to-band emission at RT. The based design of GaN LEDs is shown in **Figure 1.1-2**.

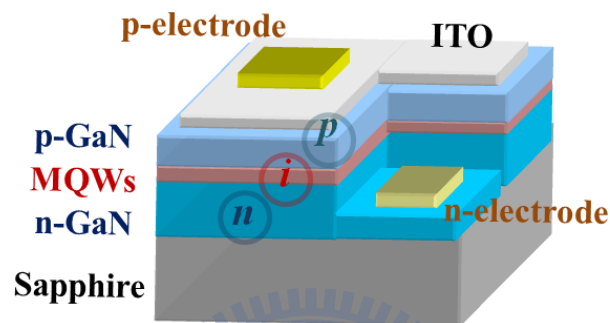


Figure 1.1-2 The schematic drawing of InGaN LED.

1.2 Nonpolar and Semipolar III-Nitride Light-Emitting Diodes: Achievements and Challenges

Current commercially available III-nitride based optoelectronic devices typically consist of epitaxial multilayer thin films grown along the polar c direction of the würtzite crystal structure. As the spectral range of light emission was extended from blue to green or red, we encountered a problem in luminescence efficiency (**Figure 1.2-1**).

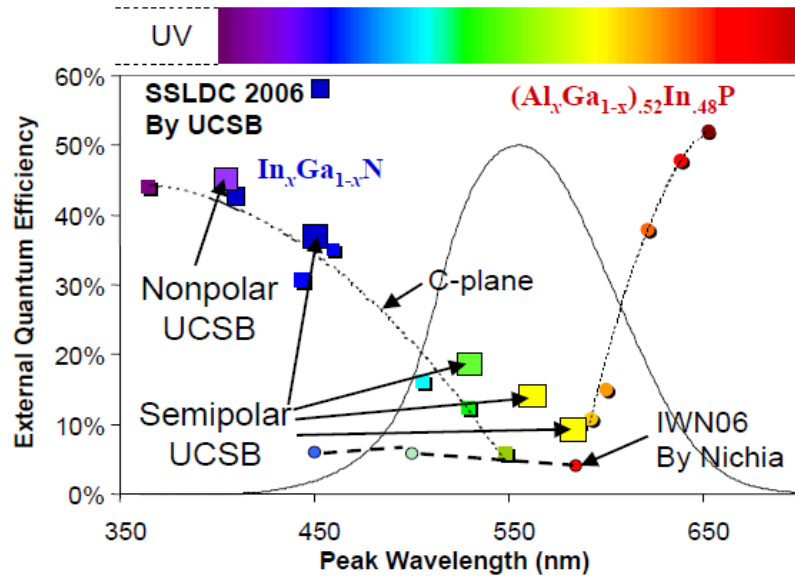


Figure 1.2-1 The external quantum efficiency (EQE) bench mark of III-V semiconductor among visible light region.

Figure 1.2-1 shows the external quantum efficiency (EQE) bench mark with different emission peak wavelength. The EQE drastically decreases from UV to green and from red to green, which is so-called efficiency green gap. There are many factors have effect on EQE from fabrication flow chart of LED:

$$\eta_{EQE} = \eta_{IQE} \times \eta_{Ext} \times \eta_{Elect} \quad (1.2-1)$$

where η_{EQE} is the EQE, η_{IQE} is the internal quantum efficiency (IQE), η_{Ext} is the light extraction efficiency, η_{Elect} is the electrical loss.

Table 1.2.1 shows the standard red, green and blue LEDs efficiency of 12 mil chip size at injected current 20 mA with carrier density about $2 \times 10^{17} \text{ cm}^{-3}$. If the IQE of green LED could be improved the realization of full collar LED is very promising.

	η_{EQE}	η_{IQE}	η_{Ext}	η_{Elect}
Red	53 %	80 %	70 %	95 %
Green	23 %	30 %	80 %	95 %
Blue	57 %	75 %	80 %	95 %

Table 1.2-1 The efficiency of 12 mil standard red, green and Blue LED at injected current 20 mA with carrier density about $2 \times 10^{17} \text{ cm}^{-3}$.

As has been reported [15], due to the strong polarization field caused by the strained InGaN layer in the c-plane, the Quantum Confined Stark Effect (QCSE) is induced which distort the energy band diagram. Therefore, it reduce the wave function overlap between the electron and hole as well as the radiative recombination. Moreover, the large blueshift of peak emission wavelength with increasing bias due to the carrier-induced screening of the polarization field could be observed.

To eliminate these polarization effects, growing devices on the nonpolar plane has been demonstrated. **Figure 1.2-2** shows the stimulation band diagram of polar and nonpolar QWs [16].

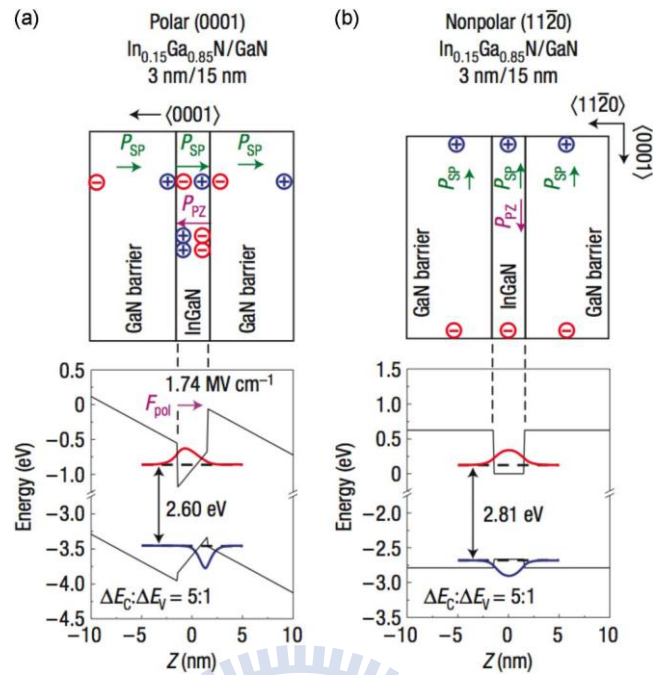


Figure 1.2-2 The QW structures on (a) polar and (b) nonpolar orientations and their band diagrams.

In 2006, Romanov et al. [17] calculated polarization charge density in InGaN QWs as a function of tilt angle of the growth plane with respect to the c-plane (**Figure 1.2-3**). Notice that semipolar planes provide a reasonable approach to reduce the polarization field. For blue or green LEDs, UCSB has already used nonpolar m-plane and semipolar {10-11} GaN substrate to enhance the EQE (**Figure 1.2-1**).

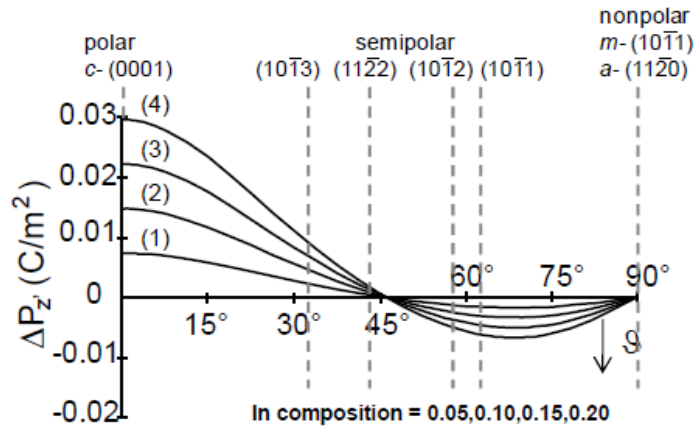
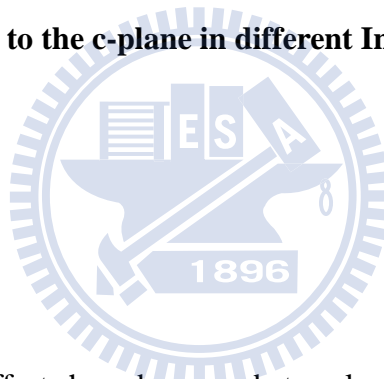


Figure 1.2-3 The polarization charge density as a function of tilt angle of the growth plane with respect to the c-plane in different In composition InGaN QWs.



1.3 Motivation

To date, tremendous efforts have been made to solve QCSE obstacle by using the nonpolar InGaN/GaN structure grown on various substrates [18]. However, the heteroepitaxy of nonpolar GaN still suffers from highly threading dislocation density (TDD), and the ideal solutions for the green efficiency gap is still lacking [18-19]. GaN based nanorod LEDs is an attractive approach towards achieving high efficiency LEDs [20-22].

GaN based nanorod LEDs possess lower extended defect, accommodate the large lattice mismatch between sapphire substrate and GaN epilayer [23-25], and highly light extraction structure properties [20-21].

The nano-fabrication technology can attract such considerable interest and be widely used in optoelectronic and electronic devices because it has large different optical and electrical properties with those in the bulk materials. It is also reported that nano-fabrication technology device had great potential for better quantum confinement and strain relaxation effect [26].

GaN nanorods technology is one of the famous nano-structure which has been produced by various fabrication methods. In 1997, Han et al. first proposed synthesizing GaN nanorods by using carbon nanotubes as templates [27]. The dimension of the synthesized GaN nanorods could be up to 25 μm in length and ranging from 4 to 50 μm in diameter. However, it is not a simple method for produce GaN nanorods.

The growth of single-crystal GaN nanorods by hybrid vapor-phase epitaxy [28] has been developed by Kim et al. A mask-free simple process by inductively coupled plasma-reactive ion etching (ICP-RIE) dry etching to fabricate GaN nanorods was proposed by Yu et al. [29]. The growth of GaN nanorods by using ferrocene as the catalyst, so-called vapor–liquid–solid (VLS) mechanism, was also demonstrated [30]. Fabrication of GaN nanorods by e-beam patterning and ICP etching was proposed by Chen et al. [31].

With the rapid development of the nano-structure fabrication techniques, these technologies had also been used in GaN devices. Johnson et. al demonstrated a single GaN nanowire lasing phenomenon in [32]. It is the first demonstration of single GaN

nanowire laser. Han et. al. performed the photoconduction studies on GaN nanowire transistors under UV and polarized UV illumination in 2004 [33]. Besides, Kim et. al. demonstrated a high brightness LEDs by fabricating high quality, dislocation-free InGaN/GaN nanorods [34]. In 2006, Son et. al. demonstrated a UV photodetector by using a single GaN nanorod with p-n junction [35]. With the following literatures, we could know that GaN nano-structure have played an important role in optoelectronic and electronic devices, such as laser, LED and photo detector.

We choose nano imprint lithography (NIL) technique to form the nanorod structure [36]. And Semipolar {10-11} nanopyramids will generate by using a combination of selective area growth (SAG).

The nano-pyramidal geometry on GaN nanorod which the InGaN/GaN QWs are placed promotes significantly greater strain relaxation in the InGaN layer and combines the epitaxial lateral overgrowth (ELO) technique to eliminate the TDs [37]. From our previous report, the internal electric field (IEF) of MQWs which grown on {10-11} surface was much smaller than on conventional c-plane and the radiative recombination rate also became much faster [38-39]. It implies that semipolar {10-11} plane has a great potential as a growth surface to develop high indium composition LEDs and overcome the efficiency green gap of III-nitride light-emitting diodes. In this work, we report the electrical characterization and optical performance of green, olive and orange emission of {10-11} semipolar nanopyramid LED on GaN nanopillar arrays.

Chapter 2. Experimental Instruments and Methods

2.1 Transmission electron microscope (TEM)

TEM is a method of imaging where a beam of electrons are directed through a sample after which they are scattered into discrete diffracted beams. The diffracted electron beams are then focused in the back focal plane of the objective lens. TEM may have two modes. When operated in diffraction mode, the diffraction lens is focused on the back focal plane to produce a diffraction pattern. For the imaging mode, the diffraction lens is focused on the first image plane to produce a magnified image. In addition, the beam may be allowed to pass through the sample to obtain a bright-field image however the diffracted beams produce a dark-field image.

The ray diagram (**Figure 2.1-1**) shows (a) imaging projecting a diffraction pattern and (b) projection of an image onto a viewing screen. The interaction of the electron beam with crystalline material tends to be by diffraction. The orientation of the planes of atoms in the crystal to the electron beam changes the intensity of diffraction. TEM equipment often uses a goniometer to allow the sample to be tilted to a range of angles to obtain specific diffraction conditions. Diffracted electrons are also selected using different apertures. The intensity of diffraction is a maximum at the Bragg angle, although a variation of diffraction intensity occurs with deviation from the Bragg angle. This also depends on the thickness of the specimen. The thinner the crystal sample, the further the crystal may deviate from the Bragg condition.

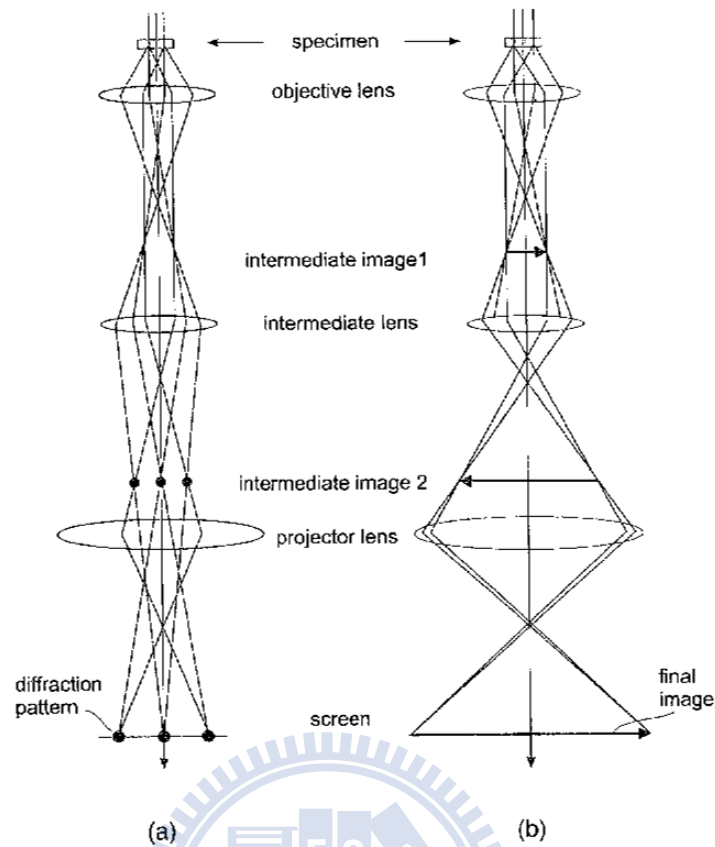


Figure 2.1-1 Ray diagram showing two basic operations of TEM.

When crystal planes are almost parallel to the electron beam they are close to fulfilling Bragg's Law. The majority of electrons are diffracted when the electron beam strikes one set of lattice planes exactly at their Bragg angle and only a few will pass through the sample undeviated. If the planes are exactly at the Bragg condition, strong diffraction will occur and the bright field image will appear dark. This variation with diffraction is shown with bend contours which are a feature of bending of the crystal planes. Dark contour images correspond to regions at the Bragg angle, while light contours result in the regions not strongly diffracting.

2.2 Photoluminescence spectroscopy (PL)

Photoluminescence characterization equipment generally uses the PL method to obtain the wavelength and intensity of the semiconductor material being analyzed. PL is the process of optical absorption of electrons in solids between an initial energy state E_i and a final energy state E_f . Excitation of an electron to E_f will leave E_i unoccupied creating a hole. Absorption creates electron-hole pairs while luminescence is the process which occurs when electrons in excited states drop to a lower level emitting a photon $\hbar\omega$ as shown in **Figure 2.2-1**. The electron-hole recombination creates a photon which is also known as a radiative transition. Direct gap materials are good light emitters and their optical properties are analyzed using this technique.

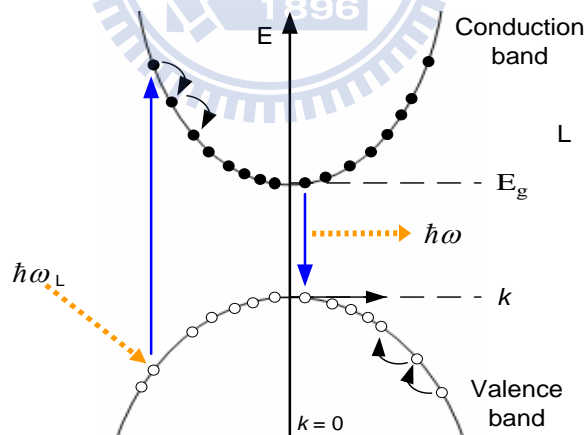


Figure 2.2-1 Interband transitions in photoluminescence system.

Photons are absorbed using an excitation source which is typically a laser. The frequency of the source $\hbar\omega_L$ must be greater than the energy gap E_g . The result is

that electrons are injected into the conduction band and holes into the valence band.

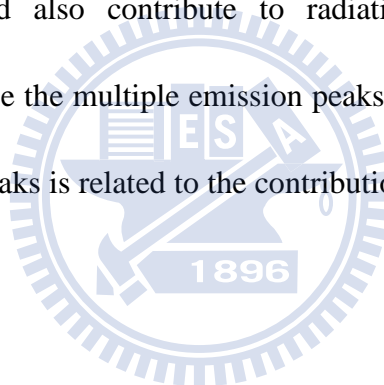
Electrons and holes are initially created in higher states within these bands but will rapidly relax to the bottom of their respective bands reaching their lowest energy state. Relaxation occurs by emitting phonons, for energy loses from the higher states, which obeys the conservation laws. The difference in energy between the two bands is E_g which is the energy gap, also known as the band gap. Luminescence occurs close to the band gap E_g , near $k = 0$. After excitation, both electrons and holes relax to their lowest energy states by emitting phonons.

PL spectroscopy has been used as a measurement method to detect the optical properties of the materials because of its nondestructive characteristics. PL is the emission of light from a material under optical excitation. The laser light source used to excite carriers should have larger energy band gap than the semiconductors. When the laser light is absorbed within the semiconductors, it would excite the carriers from the valence band to the conduction band. Then, it produces the electrons in the conduction band and the holes in the valence band. When the electron in an excited state return to the initial state, it will emit a photon whose energy is equal to the energy difference between the excited state and the initial state, therefore, we can observed the emission peak from PL spectrum.

The photoluminescence spectroscopy is the optical measurement to examine the quality and optical characteristic of material. First, when we analysis a new compound semiconductor, we can use PL measurement to know the band gap of the new material.

Second, the intensity of PL signal is contributed to the amount of radiative recombination in the materials. Therefore, PL measurement can be used to understand the material quality and the recombination mechanisms of the materials.

The carrier recombination processes occur in many ways in order to reach the equilibrium. Those processes can be divided into radiative recombination and nonradiative recombination. We can recognize the radiative recombination easily at low temperature by PL measurement, since it would not be influenced by the thermal energy. If there are some defect energy level existed in energy band gap of semiconductor, they could also contribute to radiative recombination process. Therefore, we could observe the multiple emission peaks in the PL spectrum, and the intensity of the emission peaks is related to the contribution of the individual radiative recombination process.



2.2.1 Power dependent and temperature dependent PL

For excitation power and temperature dependent PL measurement, the laser source used in this research is femto-second-pulse Ti:sapphire. The output laser wavelength could be tuned to be around 760-820 nm by adjusting the internal resonant length and gain profile. A frequency doubler and tripler crystal is setup at the laser output optical path. Here, we adopted the doubler crystal to have a wavelength at around 380-410 nm could be obtained. It is specifically important in avoiding the absorption of GaN material itself and ensured most of the injected laser photons could

excited the photons inside the MQWs. We note that this assumption essential while we predicted the injected carrier density. The tuned the 380-410 nm laser was then incident into the sample surface vertically. The sample was mounted in a closed-cycle He cryostat with a temperature controller which could be precisely controlled in the temperature region around 15 to 300 K. By the temperature controller with a set of wire heater, we could perform a serious of temperature-dependent experiments from 15 to 300 K. The luminescence signal dispersed through a 0.55-meter monochromator was detected by the photomultiplier tube (PMT). The setup detail of temperature dependent PL is shown in **Figure 2.2-2** and **Figure 2.2-3**.

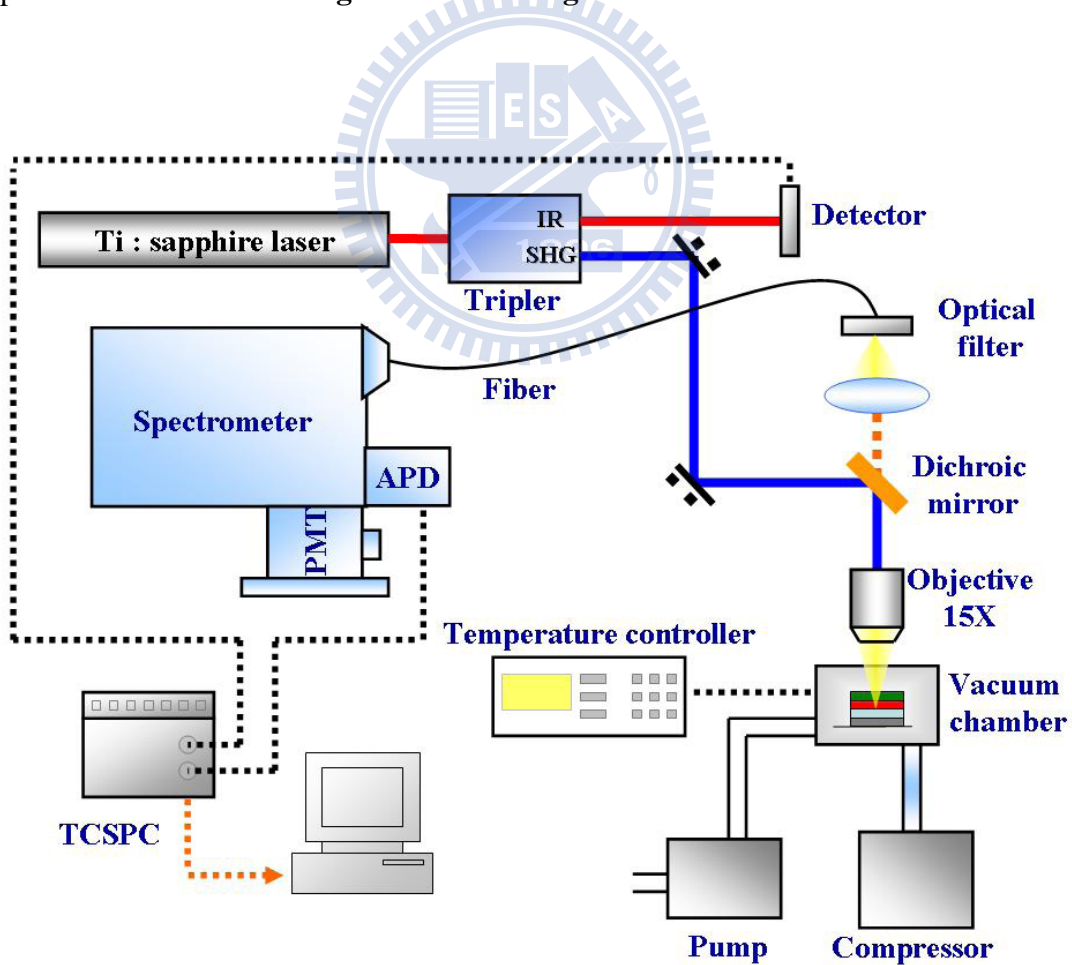


Figure 2.2-2 The schematic of PL measurement system.

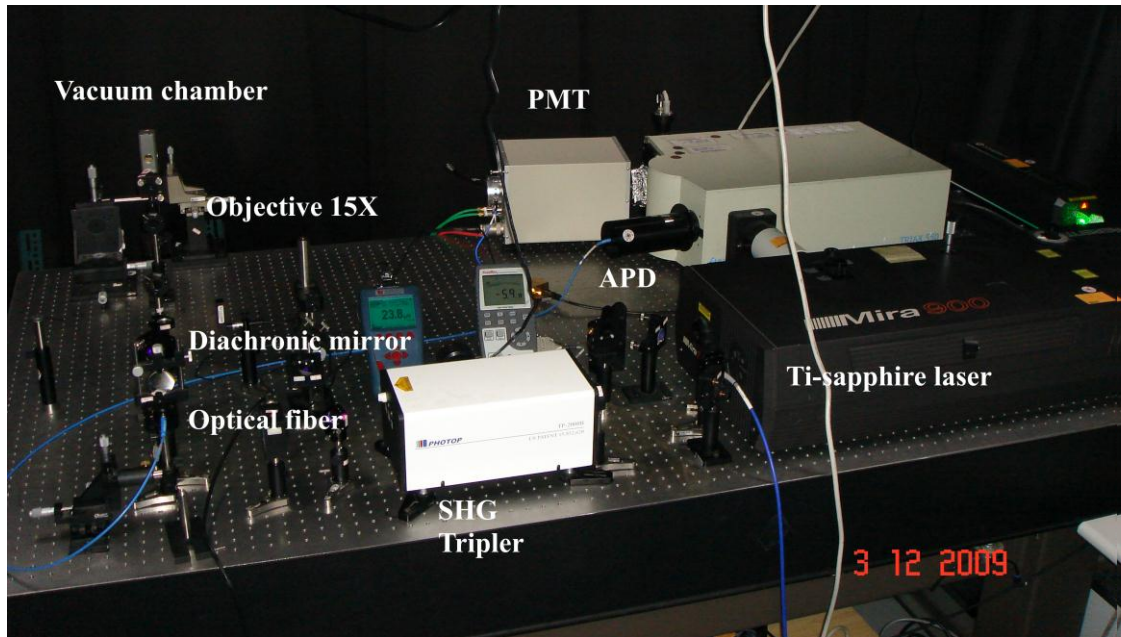


Figure 2.2-3 The picture of PL measurement system.

After the facility setup, we are then starting the optical experiments. A filter and a power meter were placed before sample chamber to modify and control the laser output power. By rotating the filter, we could vary the excitation power changing from 5×10^{-3} mW to 80 mW.

2.2.2 Time-resolved PL (TRPL)

For TRPL measurement, the laser source was same as for excitation power and temperature dependent PL measurement, which delivers ~ 150 fs laser pulses at the repetition rate of 76 MHz. And use time-correlated single photon counting (TCSPC) to calculate carrier lifetime.

TCSPC is based on the detection of single photons of a periodic light signal, the measurement of the detection times, and the reconstruction of the waveform from the individual time measurements [40-43]. TCSPC makes use of the fact that for low-level, high-repetition rate signals the light intensity is usually low enough that the probability to detect more than one signal photon in one signal period is negligible. The situation is illustrated in **Figure 2.2-4**.

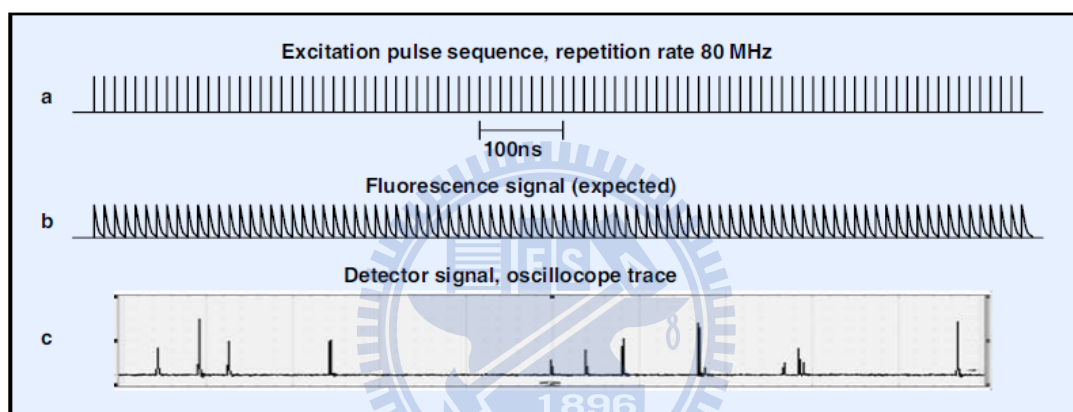


Figure 2.2-4 Detector signal for fluorescence detection at a pulse repetition rate of 80 MHz.

Fluorescence of a sample is excited by a laser of 80 MHz pulse repetition rate (a). The expected fluorescence waveform is (b). However, the detector signal measured by an oscilloscope has no similarity with the expected fluorescence waveform. Instead, it consists of a few pulses randomly spread over the time axis (c). The pulses represent the detection of single photons of the fluorescence signal. Please note that the photon detection rate of (c) is about 10^7 s^{-1} , which is on the order of the maximum possible detection rate of most detectors. Thus, the fluorescence waveform (c) has to be

considered a probability distribution of the photons, not anything like a signal waveform. Moreover, Fig. 21 shows clearly that the detection of a photon in a particular signal period is a relatively unlikely event. The detection of several photons in one signal period is even less likely. TCSPC therefore neglects the detection of several photons per signal period. The principle is shown in **Figure 2.2-5**.

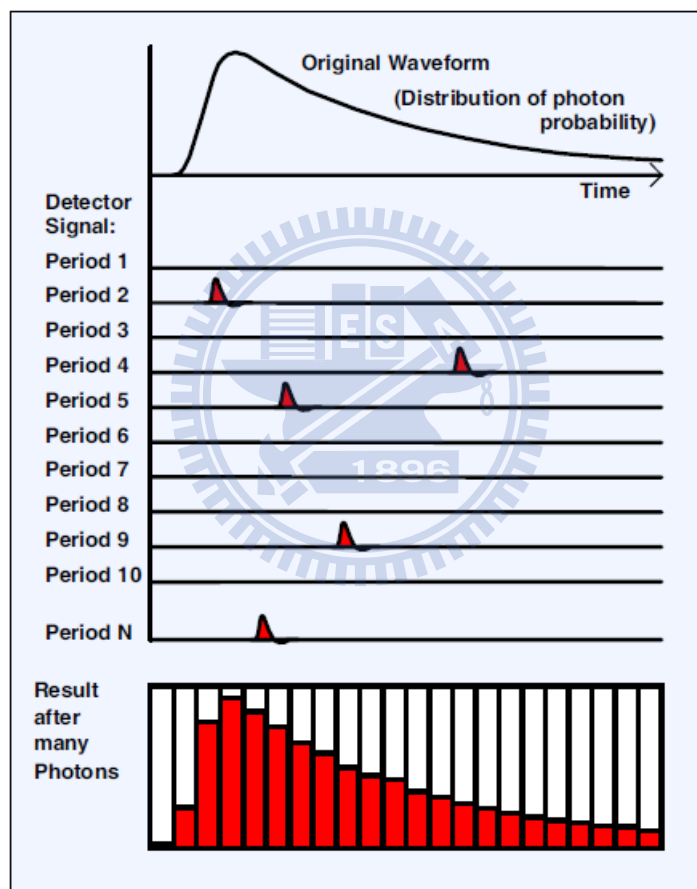


Figure 2.2-5 Principle of TCSPC.

As shown above in **Figure 2.2-4**, the detector signal consists of a train of randomly distributed pulses corresponding to the detection of the individual photons.

There are many signal periods without photons, other signal periods contain one photon pulse.

When a photon is detected, the arrival time of the corresponding detector pulse in the signal period is measured. The events are collected in a memory by adding a '1' in a memory location with an address proportional to the detection time. After many signal periods a large number of photons has been detected, and the distribution of the photons over the time in the signal period builds up. The result represents the 'waveform' of the optical pulse. (Please note that there is actually no such waveform, only a distribution of the photon probability, see **Figure 2.2-4.**) The setup detail of TRPL is shown in **Figure 2.2-2.**

2.3 Electroluminescence spectroscopy (EL)

Electroluminescence (EL) is an optical phenomenon and electrical phenomenon in which a material emits light in response to an electric current passed through it, or to a strong electric field. This is distinct from light emission resulting from heat (incandescence), chemical reaction (chemiluminescence), sound (sonoluminescence), or other mechanical action (mechanoluminescence).

Electroluminescence is the result of radiative recombination of electrons and holes in a material (usually a semiconductor). The excited electrons release their energy as photons - light. Prior to recombination, electrons and holes are separated either as a result of doping of the material to form a p-n junction (in semiconductor

electroluminescent devices such as LEDs), or through excitation by impact of high-energy electrons accelerated by a strong electric field (as with the phosphors in electroluminescent displays).

Figure 2.3-1 shows the schematic of electroluminescence measurement systems. A set of instruments including CW current source Kiethley 238, a microscope to observe the patterned electrode of sample surface, three axial stages for probe and fiber to detected the light output, and then the light detected by a 0.32 m monochromator (Jobin-Yvon Triax-320) with 1800, 1200, and 300 grooves/mm grating and the maximum width if the entrance slit was 1 mm. **Figure 2.3-2** shows the photograph of electroluminescence measure system.

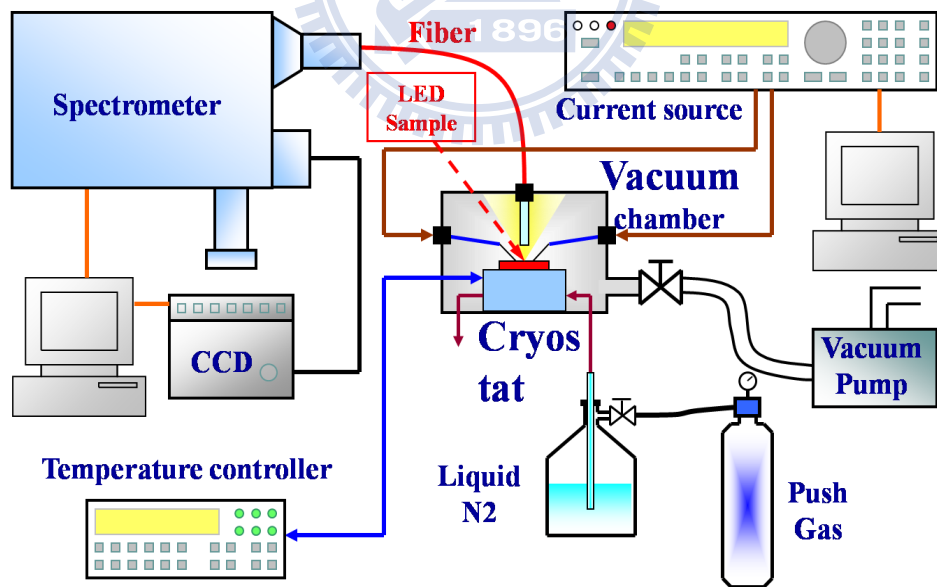


Figure 2.3-1 The schematic of EL measurement system.

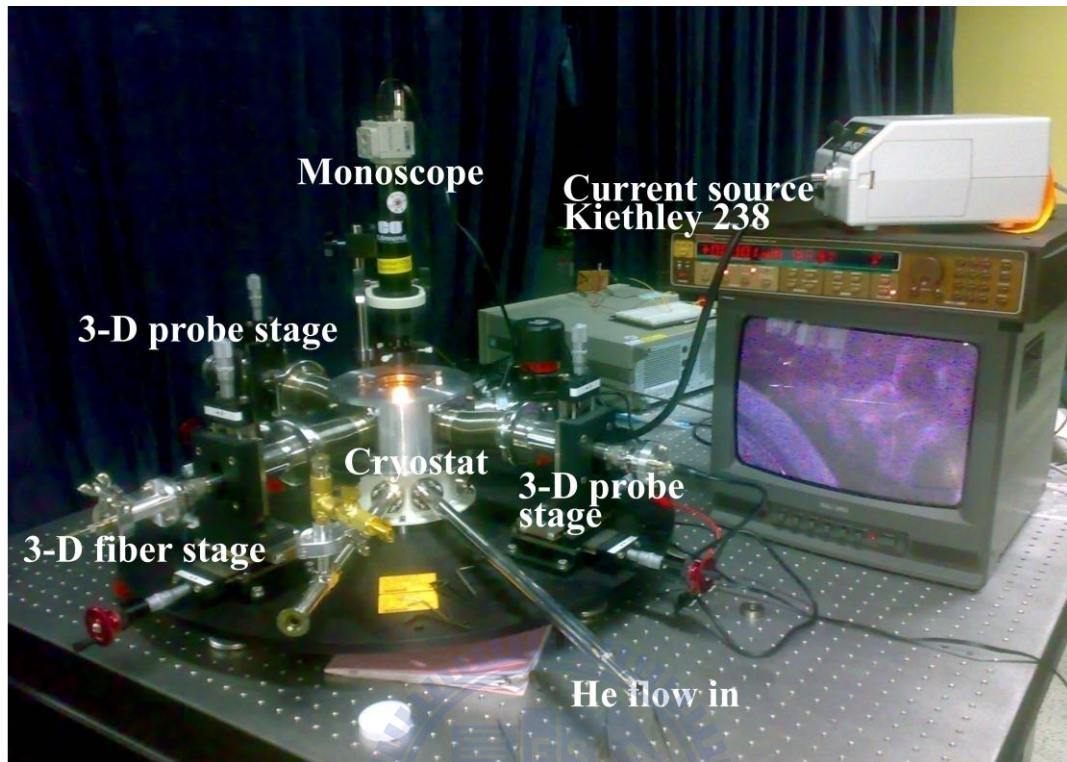


Figure 2.3-2 The picture of EL measurement system.

2.4 Scanning Electron Microscope-Cathodoluminescence (SEM-CL)

The electron microscope uses electromagnetic lenses to focus the beam to produce an image. However, SEM and TEM differ in the way images are produced and magnified. SEM is used to view the surface or near surface of a sample, whereas TEM provides information of the internal structure of thin specimens. The scanning electron microscope as the name suggests scans across the specimen by the scan coils.

As the sample is scanned by the electron beam as shown in **Figure 2.4-1**, it emits electrons and electromagnetic radiation. A detector counts the low energy secondary electrons (< 50 eV) or other radiation emitted. The image is produced by two

dimensional intensity distributions by scanning a cathode ray tube (CRT) spot onto a screen and modulating the brightness by the amplified current from the detector. Three dimensional samples change the way electrons are emitted and results in the appearance of a three dimensional image. Resolutions less than 1 nm may be achieved.

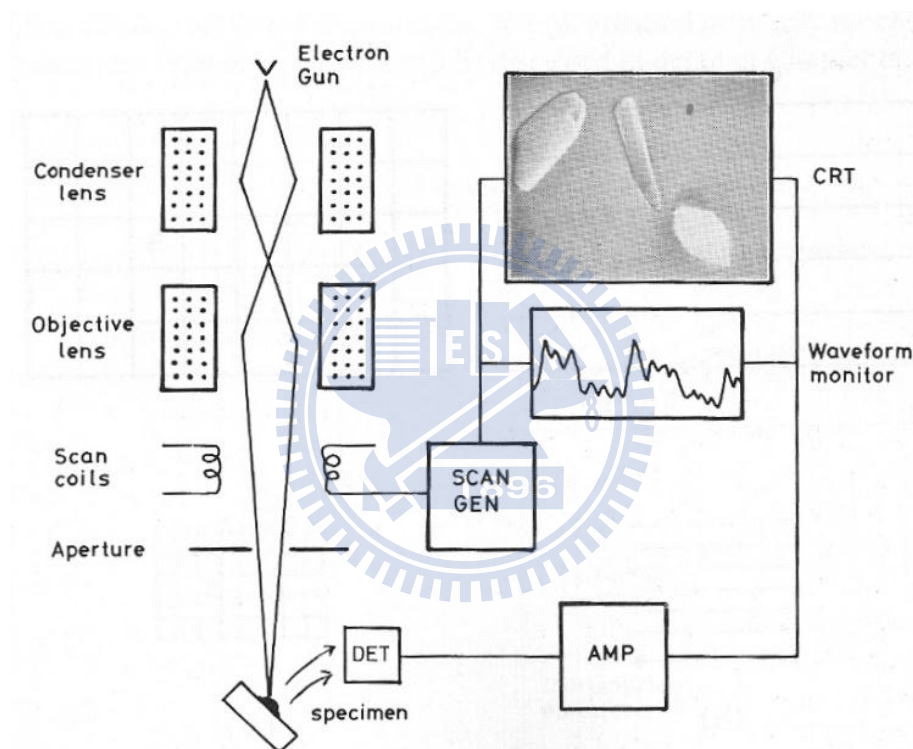


Figure 2.4-1 Schematic diagram of a scanning electron microscope.

Chapter 3. Sample structure and fabrication

In this chapter, we illustrate the fabrication flow charts of semipolar {10-11} nanopyramids LED. Moreover, the Crystalline quality analysis will be discussed by transmission electron microscope (TEM) measurement.

3.1 Fabrication of GaN nanopyramids with semipolar {10-11} InGaN/GaN

MQWs

The GaN-based material was grown by a low pressure Metal-Organic Chemical Vapor Deposition (MOCVD) system. A 2 μm thick GaN layer was first grown on a 2-inch C-plane (0001) sapphire substrate. The GaN contained 1 μm undoped GaN and 1 μm n-type GaN and were grown at 1150°C and 1160°C, respectively.

The nanorod patterns were formed by nano imprint lithography (NIL) technique. First, a 400 nm SiO_2 layer and a 200 nm polymer layer were deposited as the masks during the process. Then a patterned mold was placed onto the dried polymer film. Under a high pressure, the substrate was heated over the glass transition temperature (T_g) of the polymer. After that, the substrate and the mold were cooled down to room temperature to release the mold. After generating nanorod patterns on the polymer layer, the patterns were then transferred into SiO_2 layer by reactive ion etching (RIE) with CHF_3/O_2 mixture, and into GaN layer by inductively coupled plasma etching

(ICP) with Cl_2/Ar mixture. The mask layers were removed at the end of processes.

Figure 3.1-1 shown the flow chart of nano imprint lithography (NIL).

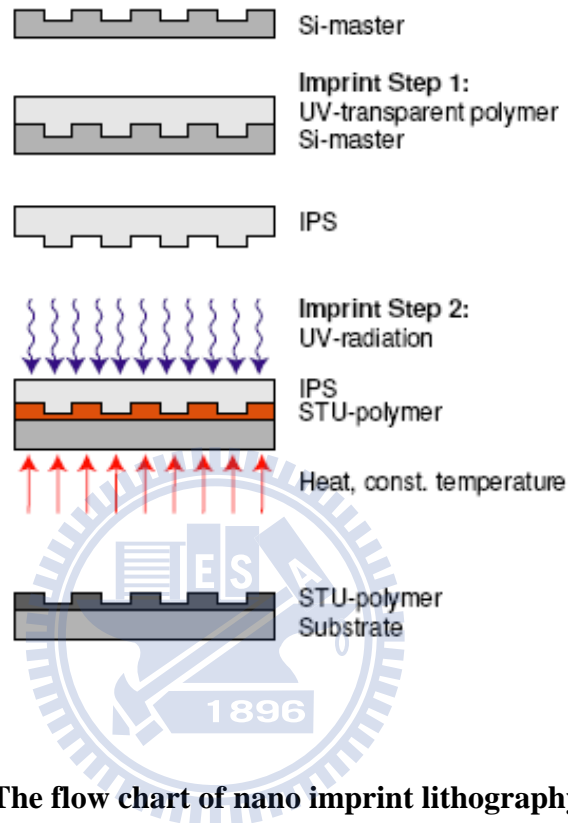


Figure 3.1-1 The flow chart of nano imprint lithography (NIL).

Before the regrowth process, the sample was passivated with porous SiO_2 at sidewall. The pyramid shape n-type GaN structures were regrowth on the top of GaN nanopillars at 730°C by using a combination of selective area growth (SAG). The 450 nm height pyramids contain 10-pair $\text{In}_{0.3}\text{Ga}_{0.7}\text{N}/\text{GaN}$ (3nm/8nm) multiple quantum wells (MQWs), which support the emission around 500 nm wavelength. The fabrication procedure was shown in **Figure 3.1-2**.

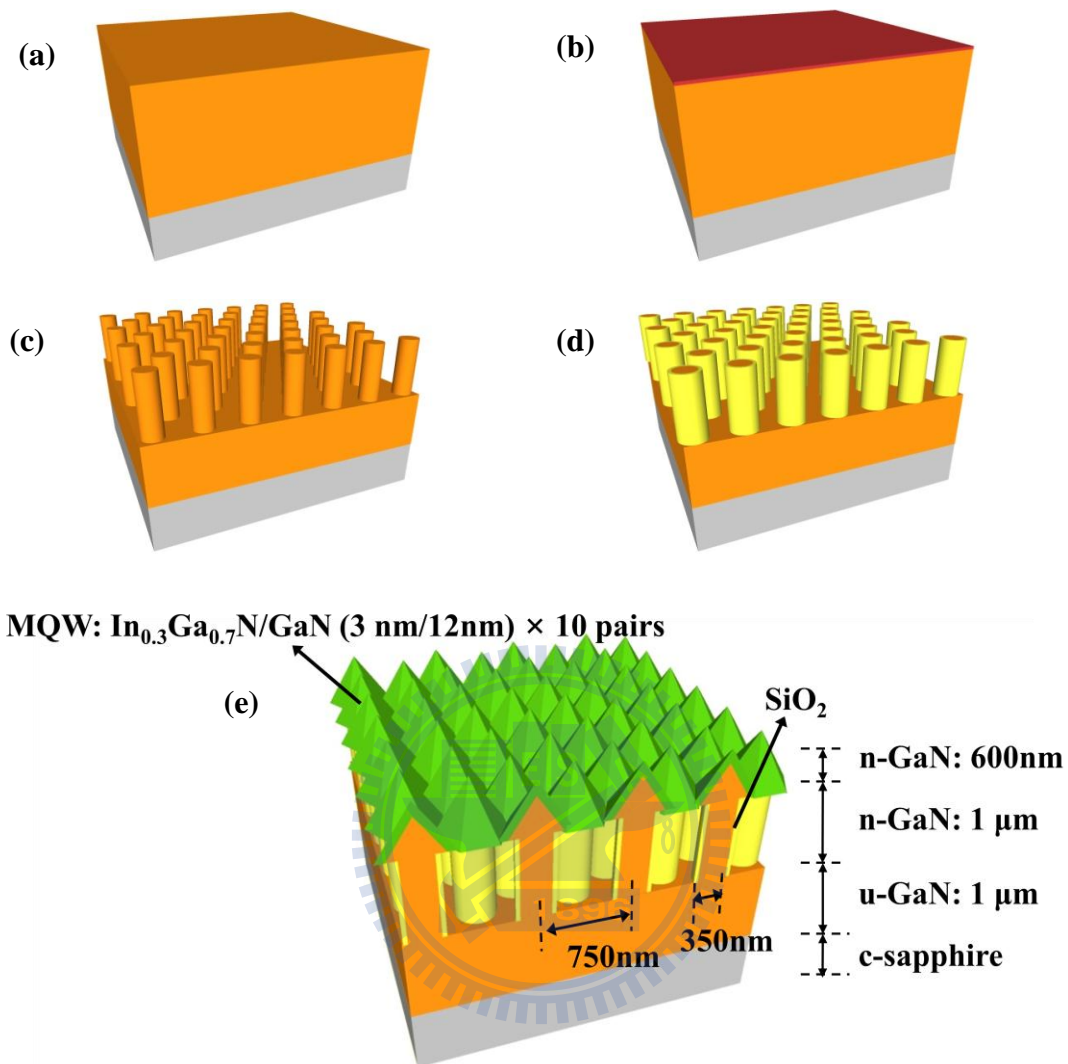


Figure 3.1-2 Illustrations of fabrication process of nanopyramid MQWs. (a) GaN template contained 1 μm undoped GaN and 1 μm n-type GaN. (b) A 400 nm SiO_2 layer and a 200 nm polymer layer were deposited. (c) Nanorod patterns were formed by nano imprint lithography (NIL) technique. (d) Passivated with porous SiO_2 at sidewall. (e) Schematic structure of GaN-based nanorod structure with the regrowth of semipolar {10-11} GaN pyramids and 10-pair $\text{In}_{0.3}\text{Ga}_{0.7}\text{N}/\text{GaN}$ (3nm/12nm) MQWs.

The diameter and the pitch of GaN nanorod was 350 nm and 750 nm, respectively. And the etch depth of the nanopillars is approximately 1 μm . **Figure 3.1-3** shows the angle-view SEM images of (a) GaN nanorod. (b) GaN nanorod with sidewall passivation. (c) GaN nanopillars with semipolar $\{10\text{-}11\}$ $\text{In}_{0.3}\text{Ga}_{0.7}\text{N}/\text{GaN}$ MQW.

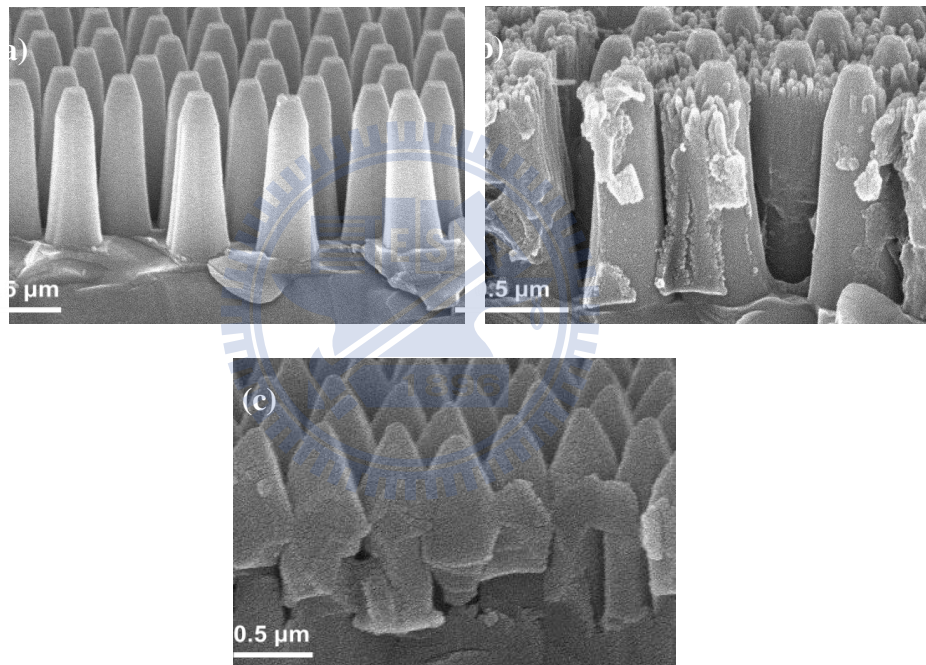


Figure 3.1-3 The angle-view SEM images of (a) GaN nanorod arrays. (b) GaN nanorod with sidewall passivation. (c) GaN nanopillars with semipolar $\{10\text{-}11\}$ $\text{In}_{0.3}\text{Ga}_{0.7}\text{N}/\text{GaN}$ MQW.

Finally, the complete epitaxial structure then underwent a standard four-mask LED fabrication processing with ITO current spreading layer and Ni/Au contact metal depositions, into an LED structure with a mesa size of $300 \times 300 \mu\text{m}^2$. **Figure 3.1-4** shows the illustration of nanopyramid LED device.

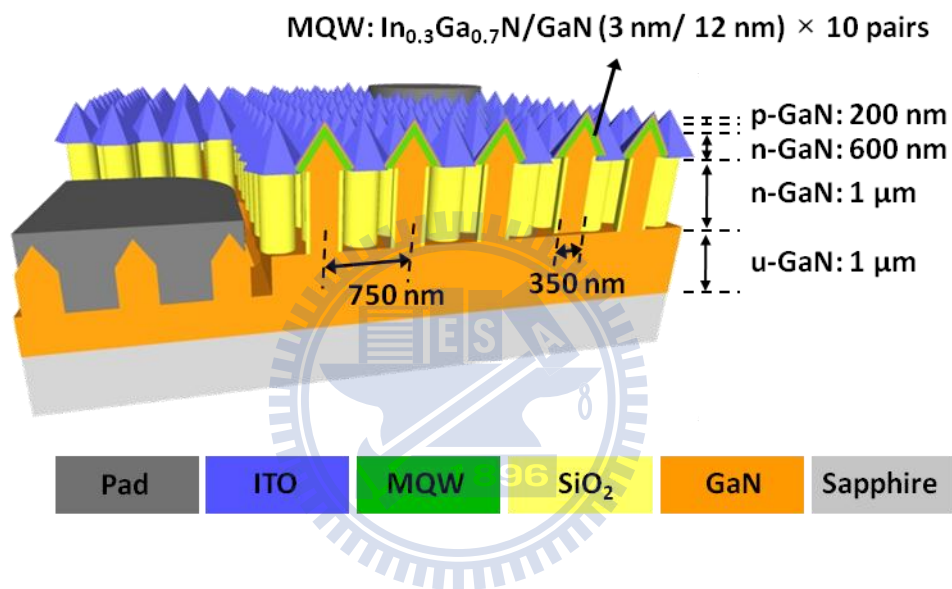


Figure 3.1-4 Illustration of nanopyramid LED device.

3.2 Crystal quality analysis of the semipolar {10-11} InGaN/GaN multiple quantum wells (MQWs)

The TEM measurement was used to confirm the quality of semipolar {10-11} MQWs (Figure 3.2-1). The angle between the MQWs and c-plane was 62° , and the inclined surface was the semipolar {10-11} facet. There existed air voids around GaN

nanorods can act as waveguides that improve light extraction [44]. **Figure 3.2-1 (b)** shown TEM enlarge view of semiolar $\{10-11\}$ MQWs. The interface of MQWs was smooth and the thickness of InGaN well and GaN barrier from apex to bottom of the nanopyramid were nearly uniform, which were 2 and 8 nm, respectively.

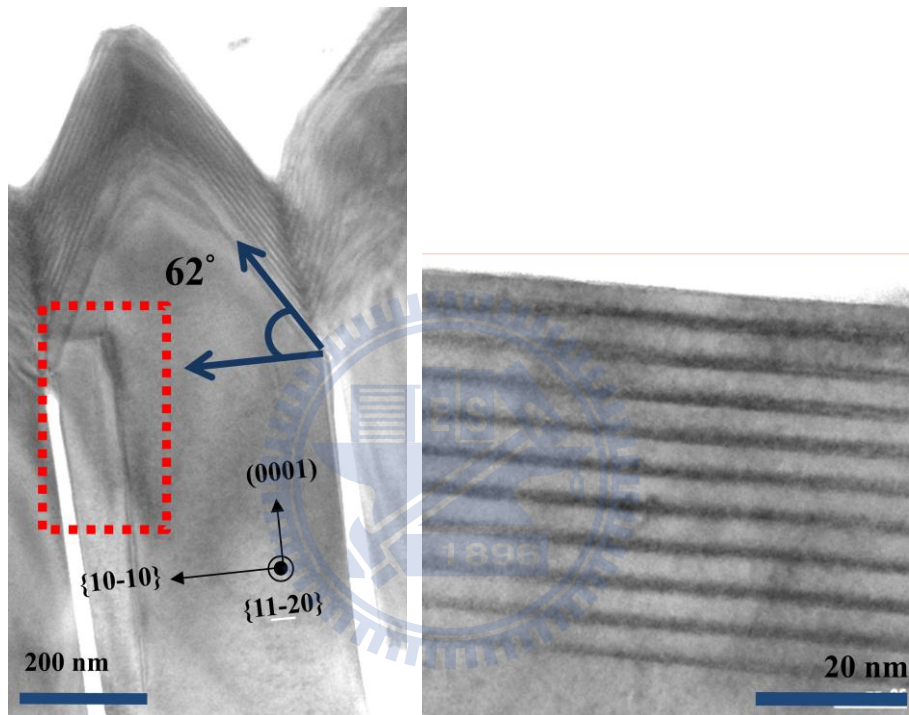


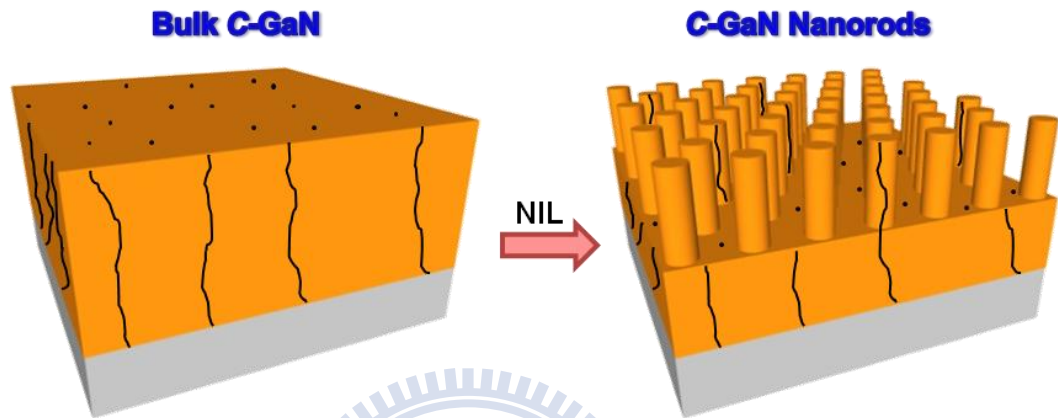
Figure 3.2-1 The TEM images of (a) GaN nanorod with semipolar nanopyramids.
(b) Enlarge view of semiolar $\{10-11\}$ MQWs.

The mechanism of reduce threading dislocation density (TDD) in semipolar $\{10-11\}$ MQWs was shown in **Figure 3.2-2**. First, threading dislocations in bulk c-GaN were suppressed by nano imprint lithography (NIL). Moreover, threading dislocation was bended by epitaxy lateral overgrowth (ELO) process. Finally,

reduction of threading dislocation density (TDD) in MQWs can be observed in

Figure 3.2-1.

(a)



(b)

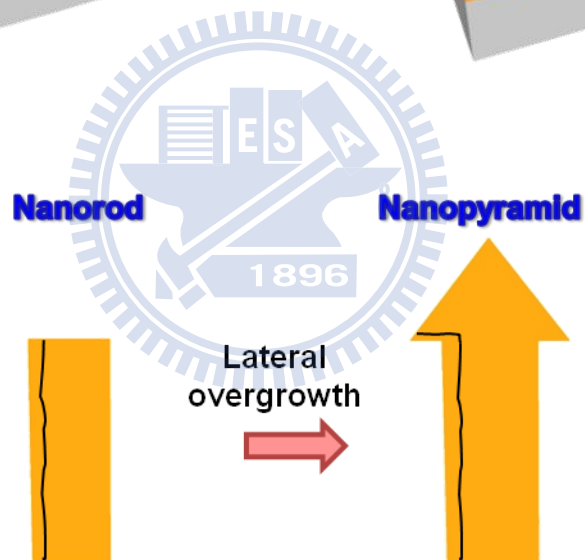


Figure 3.2-2 The mechanism of reduce threading dislocation density (TDD) in semipolar {10-11} MQWs by (a) nano imprint lithography (NIL) and (b) epitaxy lateral overgrowth (ELO).

From the result of TEM measurement, the SAE is a promising technique to fabricate high crystalline quality semipolar {10-11} MQWs.

3.3 Spatial resolved cathodoluminescence (CL) of nanopyramid structure

To investigate the Indium content distribution on the nanopyramids surface, the scanning electron microscope (SEM) and spatial resolved cathodoluminescence (CL) measurement was applied.

Figure 3.3-2 (a) shows the top view SEM image of the semipolar MQWs. The diameter of GaN nanopyramid is around 300 nm. And the CL spectrum was shown in **Figure 3.3-1**. To investigate the spatial distribution of emission wavelength, we collected the emission signal at fixed emission wavelength, which were 460, 480, 500, 520, 540, 560 and 580 nm, respectively (**Figure 3.3-2 (b)~(h)**). The peak emission wavelength at about 500 nm, corresponding to the PL measurement, came from the sidewall facets of pyramids. As shown in the figures, the emission wavelength became longer from base region to the apex of pyramid, which was dominated by gas phase diffusion process under our growth condition [45-46]. These results shown that higher Indium content was formed by the geometrical structure and growth condition.

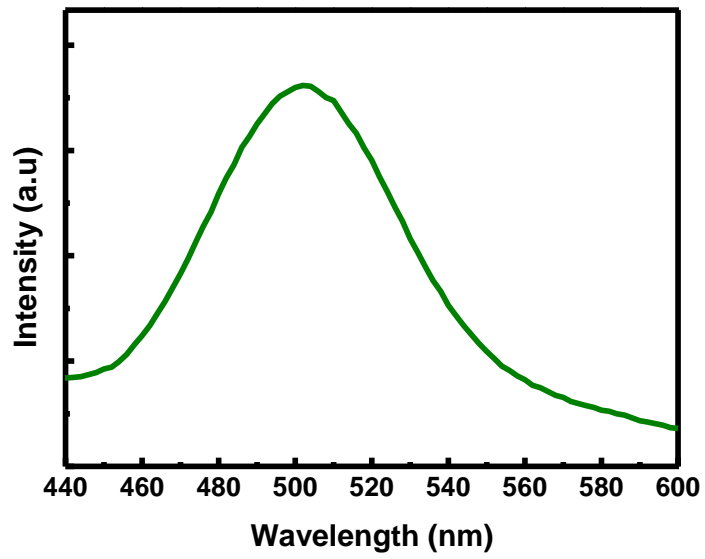
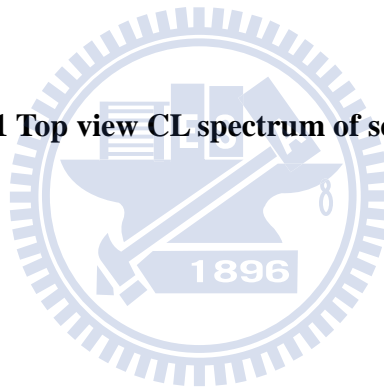


Figure 3.3-1 Top view CL spectrum of semipolar MQWs.



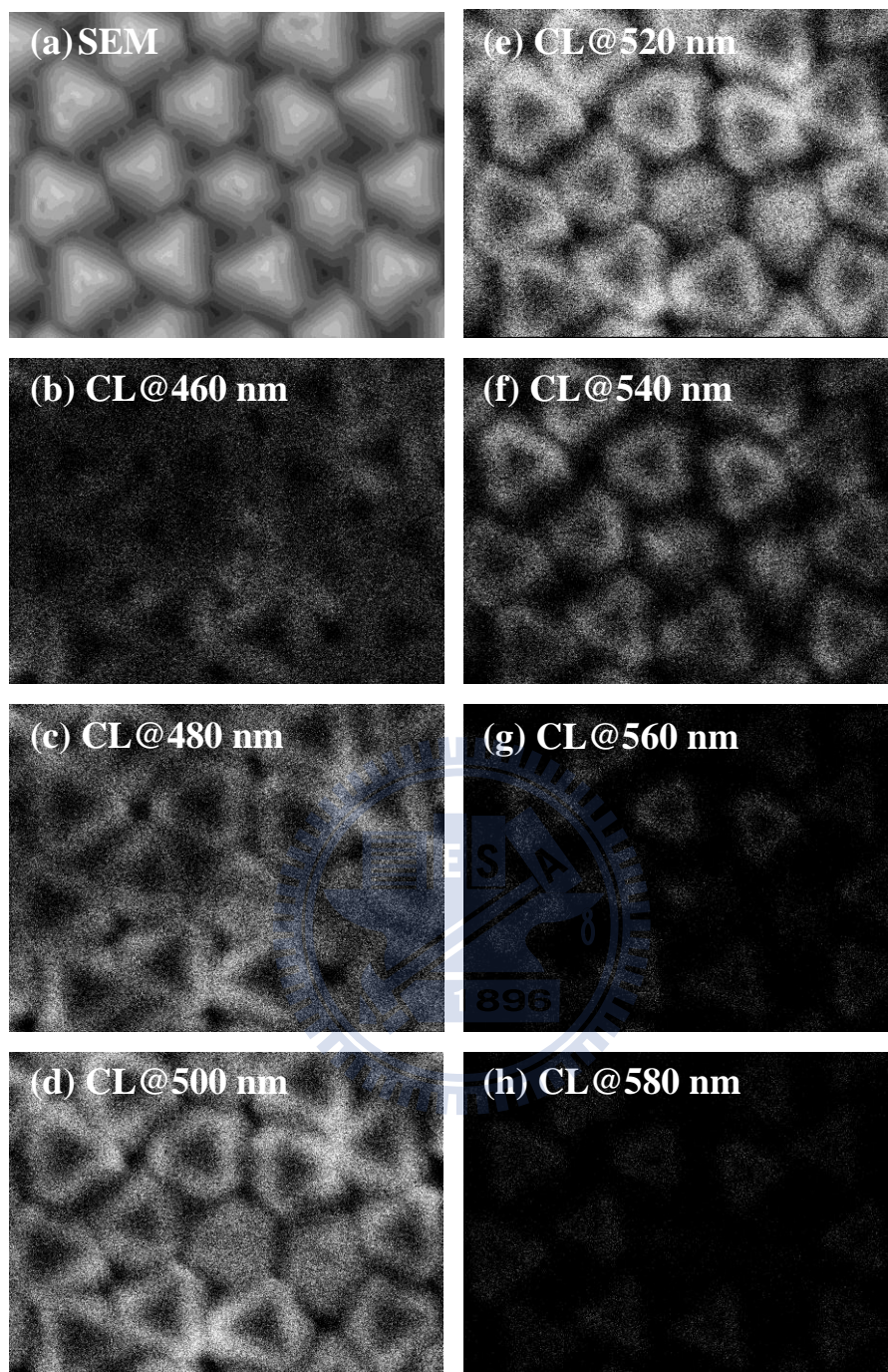


Figure 3.3-2 (a) Top view SEM image. CL emission signal at fix emission wavelength (b) 460 nm, (c) 480 nm, (d) 500 nm, (e) 520 nm, (f) 540 nm, (g) 560 nm and (h) 580 nm, respectively.

Chapter 4. Optical Analysis of Polar and Semipolar MQWs

In this chapter, in order to identify the reduction of quantum confined Stark effect (QCSE), we estimated the magnitude of internal electron field (IEF) and the internal quantum efficiency (IQE) of semipolar and c-plane MQWs (same emission wavelength about 500 nm) by measuring the power dependent photon luminescence (PL) at low (20K) and room temperatures, investigated energy band diagram of semi-polar and c-plane QW structure by simulation, and discussed the carrier dynamic by time-resolved photoluminescence.

4.1 Investigation of internal electron field (IEF)

To identify the reduction of QCSE for the semipolar MQWs, we estimated discuss the internal electric field (IEF) of the c-plane and the semipolar MQWs by measuring the power dependent photon luminescence (PL) at T=15 K.

4.1.1 Introduction

Several research groups have reported that the internal electric field existed (IEF) in InGaN/GaN QW structures [47-49]. This internal electric field tilts the potential band across the QW, resulting in a redshift of wavelength and spatial separation of electrons and holes. This is called the QCSE.

The QCSE is most often studied by the photoluminescence (PL) spectroscopy.

The magnitude and penetration of the electric field is determined by the total band bending, the carrier density, and the dielectric constant. In a PL experiment, free carriers are generated close to the surface by the exciting light (typically a laser), and are separated by the built-in surface field, which results in a reduction of the initial electric field. By varying the excitation power, the electric field “felt” by the QW’s is modified and consequently, the PL peak position is shifted as described by the QCSE. When the excitation power is low, the electric field in the sample is high, therefore, the energy of the PL peak is significantly shifted from its theoretical (zero field) value. As the excitation power is increased, the internal field is reduced, thus the PL peak moves towards the hypothetical “no field” position. As the internal field tends towards the flat-band condition with increasing light output power, the increase in the PL peak energy is reduced. For most samples, therefore, we expect to see a power dependent PL spectrum, characterized by an increase in the energy of the PL peak with excitation power, and a saturation of the PL peak position at high power as the surface field tends towards the flat-band condition.

4.1.2 Calculation

In the following, we shall derive an expression for the internal field-induced PL peak shift in terms of the built-in electric field, the excitation intensity, and the temperature.

The magnitude of the surface electric field in a semiconductor can be calculated

using the model developed by Kanata et al. [50]:

$$F_s = \left(\frac{-2V_s \rho}{\epsilon \epsilon_0} \right)^{1/2} \quad (4.1-1)$$

where F_s is the surface electric field, V_s is the equilibrium surface voltage, ρ is the net charge density, ϵ is the low-frequency dielectric constant, and ϵ_0 is the permittivity of free space.

Now, we consider the energy band diagram of a p-n junction under the exciting light, shown in **Figure 4.1-1(a)**. It is assumed to have ideal I-V characteristics. The equivalent circuit is shown in **Figure 4.1-1(b)**, where a constant current source is in parallel with the junction. The source I_L results from the excitation of excess carriers by the exciting light; I_s is the diode saturation current, and R_L is the load resistance.

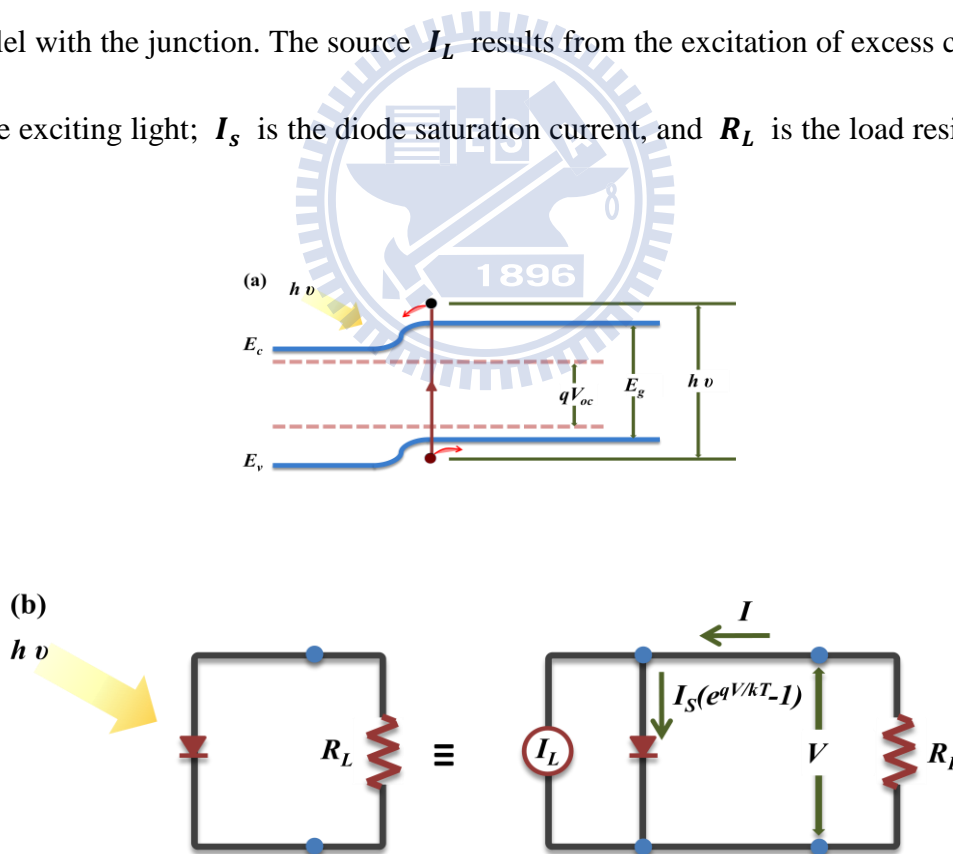


Figure 4.1-1 (a) Energy band diagram of a p-n junction under exciting light.

(b) Idealized equivalent circuit.

The I-V characteristics of such a device are given by

$$I = I_s(e^{qV/kT} - 1) - I_L \quad (4.1-2)$$

Under steady-state conditions, an expression for the surface voltage V_s in the presence of photoinduced current is given by [51]

$$V_s = V_{so} \pm \frac{kT}{e} \ln(bN + 1) \quad (4.1-3)$$

where V_{so} is the surface potential (in the dark), k is the Boltzmann constant, T is the absolute temperature, e is the electronic charge, N is the excitation rate of free carriers per unit area, and b is an intensity-independent constant given by:

$$b = \exp\left(\frac{eV_{so}}{kT}\right) \left(\frac{e}{AT^2}\right) \quad (4.1-4)$$

where A is the modified Richardson constant. The surface potential, V_{so} , has been measured by a number of research groups and its value as a function of temperature may be obtained from Ref. [52].

The parameter N is determined by the excitation intensity P [50]:

$$N \approx \frac{Pg(1-R)}{h\nu} \quad (4.1-5)$$

where g is the quantum efficiency (which is of the order of unity), R is the reflectivity coefficient of the material which, for GaN, we took as $R = 0.15$, and $h\nu$ is the photon energy of the exciting light ($h\nu = 3.1$ eV).

Using Equation (4.1-1), (4.1-3)-(4.1-5), we can calculate the internal electric field F_s as a function of the incident illumination, P :

$$F_s = \left(F_{so}^2 - \frac{F_{so}^2 kT \ln\{[bPg(1-R)/h\nu] + 1\}}{eV_{so}} \right)^{1/2} \quad (4.1-6)$$

Assuming that the electric field is constant over the undoped QW region, it is

this electric field which, by way of the QCSE, modifies the PL emission originating from QW's. As we see from **Equation (4.1-6)** the internal field is a nonlinear function of the excitation intensity.

The internal field-induced PL peak shift may be calculated by using the Hamiltonian of the perturbation model. Let us consider an electron, with charge e and effective mass m^* , in an infinite quantum well of width L in the presence of the surface electric field F_s along the direction of the well, z . (The direction is perpendicular to the material layers.) The origins of distance and of electrostatic potential are chosen at the center of the well (**Figure 4.1-2**).

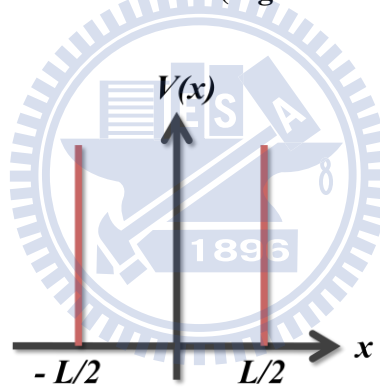


Figure 4.1-2 The infinite quantum well.

The Hamiltonian of the problem is therefore

$$H = H_0 + |e|F_s z \quad (4.1-7)$$

where H_0 is the zero-field quantum well Hamiltonian. The spectrum of H_0 is given by

$$E_n^{(0)} = \frac{\hbar^2 \pi^2}{2m^* L^2} n^2 \quad n = 1, 2, \dots \quad (4.1-8)$$

For weak fields, such that

$$|e|FL \ll \frac{\hbar^2 \pi^2}{2m^* L^2} \quad (4.1-9)$$

a second-order perturbation calculation gives for the energy shift of the ground state

[53]

$$\Delta E^{(2)} = -C' \frac{m^* e^2 F_s^2 L^4}{\hbar^2} = -C F_s^2 \quad (4.1-10)$$

with

$$C' = \frac{2^9}{\pi^6} \sum_{p=1}^{\infty} \frac{p^2}{(4p^2-1)^5} = \frac{1}{24\pi^2} \left(\frac{15}{\pi^2} - 1 \right) \quad (4.1-11)$$

therefore

$$C = \frac{1}{24\pi^2} \left(\frac{15}{\pi^2} - 1 \right) \frac{m^* e^2 L^4}{\hbar^2} \quad (4.1-12)$$

Using **Equation (4.1-3)-(4.1-6)**, the PL peak energy at a temperature T , in the presence of an internal electric field F_{so} and an illumination intensity P , may be written as

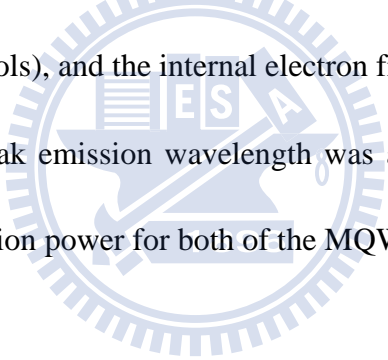
$$E_{PL} = E_0 - C \left(F_{so}^2 - \frac{F_{so}^2 k T \ln\{[bPg(1-R)/h\nu] + 1\}}{eV_{so}} \right) \quad (4.1-13)$$

where E_{PL} is the PL emission energy from the QW under illumination, E_0 is the energy of the PL peak assuming zero internal electric field, and F_{so} is the built-in field under zero illumination intensity. Note that a number of other effects were not included in our model (we neglected the two-dimensional nature of the system, carrier

distribution in the barriers and the wells, excitonic and nonradiative recombination channels, possible recombination coefficient change due to separation of the carriers in wells, etc.).

4.1.3 Experimental result and discussion

We measured the excitation power dependent PL at low temperature ($T=15$ K) for the semipolar and the c-plane MQWs, and the excitation power was changed from 5×10^{-3} mW to 80 mW. **Figure 4.1-3** shown the PL peak emission energy with different excitation power at low temperature ($T=15$ K) for c-plane and semipolar MQWs, respectively (symbols), and the internal electron field (IEF) fitting result from **Equation (4.1-13)**. The peak emission wavelength was about 500 nm and the blue shift with increasing excitation power for both of the MQWs.



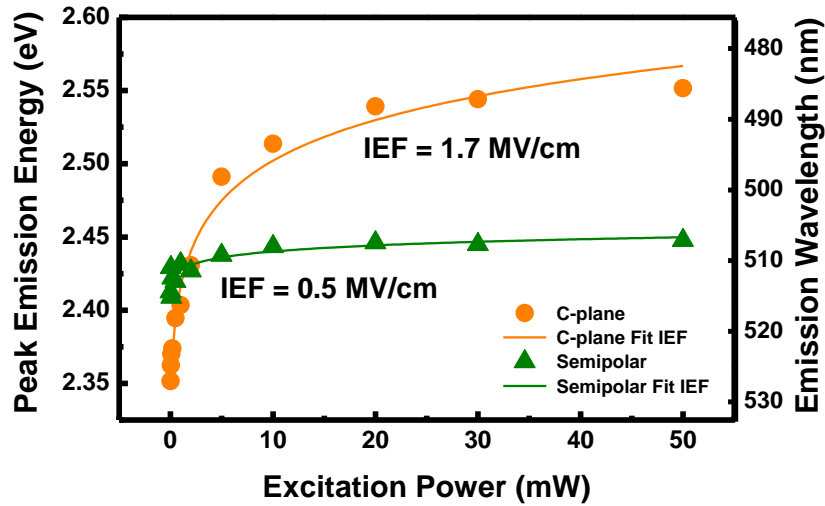


Figure 4.1-3 The PL peak emission energy with different excitation power for the semipolar and c-plane MQWs (symbols) at T=15 K. The solid lines are the internal electron field (IEF) fitting results from Equation (4.1-13).

For both of the MQWs in the low excitation power region, the emission peak blue shifts significantly, which can be assigned to band filling effect of localized state. After filled the localized state, the blue shift of both LEDs may be explained by the carrier screening of the QCSE resulted from piezoelectric fields [54-55]. It can clearly be seen that the blueshift of semipolar LED is only about 70 meV, which is much smaller than that of 200 meV in the c-plane LED's. This phenomenon indicated the internal electric field (IEF) in semipolar MQWs was much smaller than that in the c-plane LED. By fitting the experimental data with equation 4.1-13, the internal electric field (IEF) of the MQWs was found to be remarkably reduced from 1.7 to 0.5 MV/cm as changing the growth plane from c-plane to semipolar plane.

4.2 Property of the internal quantum efficiency (IQE)

We have demonstrated the reduction of the internal electric field (IEF) in the semipolar MQWs. According to the theory of QCSE, the wave function overlap between electron and hole will be enhanced, thus internal quantum efficiency (IQE) will be improved. In this section, we analysis the IQE properties with the semipolar and the c-plane MQWs.

4.2.1 Theory and measurement of IQE

The active region of ideal LED emits one photon when one electron injected. Each charge quantum-particle (electron) produces one light quantum-particle (photon). Thus the ideal active region of an LED has a quantum efficiency of unity. The internal quantum efficiency (IQE) is defined as:

$$\eta_{int} = \frac{\text{number of photons emitted from active region per second}}{\text{number of electrons injected into LED per second}} = C \frac{I_{PL}/E_{PL}}{I_{EX}/E_{EX}} \quad (4.2-1)$$

where I_{PL} and I_{EX} are PL intensity and excitation intensity, respectively. E_{PL} and E_{EX} are PL photon energy and excitation photon energy, respectively. C is a constant affected by mostly carrier injection efficiency by laser, light extraction and correction efficiency of PL, and does not depend on either excitation power density or measurement temperature.

From the theoretical of carrier dynamics, we can assume that the IQE is 100% at low temperature (LT). In order to cancel the constant C , we divide the IQE at RT by the IQE at LT, consequently, the IQE of the LED at room temperature (RT) can be

rewrite as:

$$(\eta_{int})_{RT} = \frac{\left(C \frac{I_{PL}/E_{PL}}{I_{EX}/E_{EX}}\right)_{RT}}{\left(C \frac{I_{PL}/E_{PL}}{I_{EX}/E_{EX}}\right)_{LT}} = \frac{(I_{PL})_{RT}}{(I_{PL})_{LT}} = \frac{I_{RT}}{I_0} \quad (4.2-2)$$

In the light of equation (4.2-2), we measured the excitation power dependent PL intensity at low and room temperature, and then the IQE curves as a function of excitation power and temperature can be obtained.

By rotating the filter, we can vary the excitation power changing from 5×10^{-3} mW to 80 mW. We note in every PL measurement setup, the diameter of laser spot may have different spot size. Therefore, though we can plot the relationship between the injected power and the efficiency, it will be more convenient for comparison and reflect the influence of the carrier density more clearly, if we can transfer the power into carrier density. To do that, we can follow the equation below to transfer our injected power to carrier density (n):

$$n = \frac{P}{(h\nu) \times \phi \times d_{active} \times f} \times \exp(-\alpha_{GaN} d_{GaN}) \times [1 - \exp(-\alpha_{InGaN} d_{active})] \times (1 - R) \quad (4.2-3)$$

The injected carrier density is determined primarily by the power of pumping laser (P), the energy of injected photon ($h\nu$), the spot size of pumping laser (ϕ), the thickness of GaN and active region (d_{GaN} , d_{active}), the repetition rate of pumping laser (f), the absorption efficiency of GaN and InGaN (α_{GaN} , α_{InGaN}), and the reflectance of pumping laser (R), as expressed by the following equation. We choose $\phi = 50 \mu\text{m}$, $d_{GaN} = 120 \text{ nm}$, $d_{active} = 60 \text{ nm}$ and 30 nm (semipolar and

c-plane), $\alpha_{InGaN} = 10^5 \text{ cm}^{-1}$, $f = 76 \text{ MHz}$ and $R = 0.1$ and 0.4 (semipolar and c-plane) to calculate the injected carrier density in our samples. Here we ignore the absorption of GaN since the energy of pumping photons is less than its energy bandgap, i.e. $\alpha_{GaN} = 0$.

4.2.2 Experimental result and discussion

Figure 4.2-1 and **Figure 4.2-2** shown the IQE with different injected carrier density of the semipolar and c-plane MQWs. The IQE at injected carrier density about $3 \times 10^{17} \text{ cm}^{-3}$ (same carrier density with 12 mil chip size at 20 mA) of the semipolar and c-plane MQWs was 44% and 28%, respectively. It was enhance about 57 % from the c-plane to the semipolar MQWs. This result evinced that the QCSE of the semipolar MQWs was much smaller than the c-plane MQWs, which was consistent with the internal electric field fitting result.

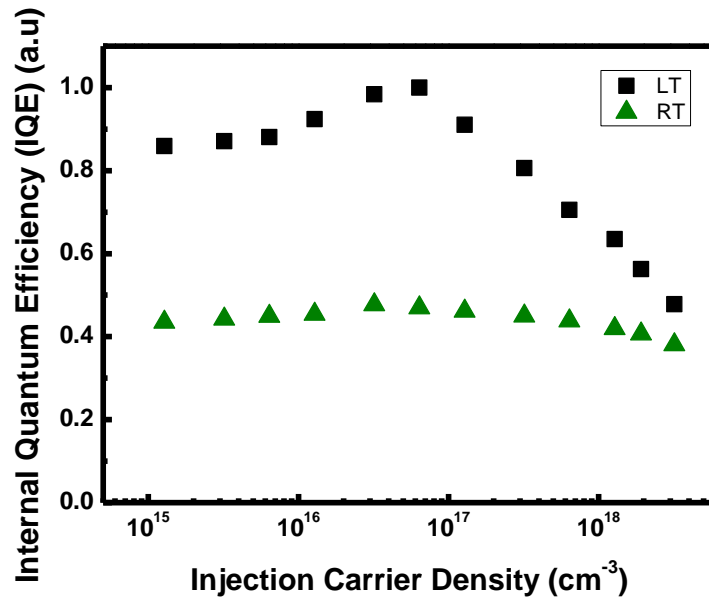


Figure 4.2-1 Internal quantum efficiency (IQE) as a function of different injected carrier density for semipolar MQWs.

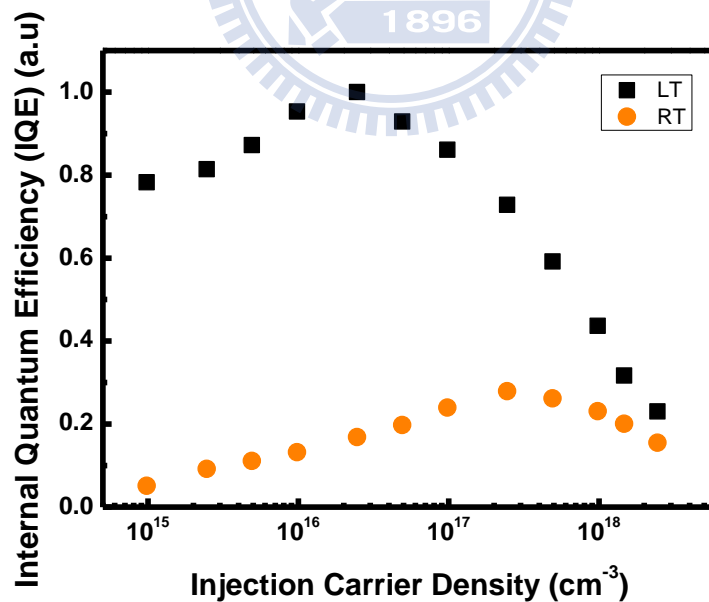


Figure 4.2-2 Internal quantum efficiency (IQE) as a function of different injected carrier density for c-plane MQWs.

To further confirm the reduction of the QCSE, the simulated of the energy band diagram was used. According to the parameters, we obtained the simulated energy band diagram (**Figure 4.2-3**). The energy band was much less distorted when the growth plane changed from c-plane to semipolar. And the wavefunction overlap of the c-plane and the semipolar quantum well (QW) are 60 % and 94 %, respectively. That is, the wavefunction overlap was enhanced about 57 % which agrees with the enhancement of IQE value mentioned above.

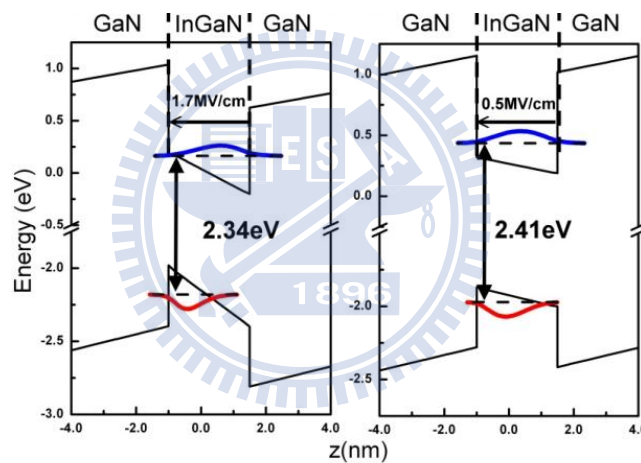


Figure 4.2-3 The simulated energy band diagram from the internal electron field fitting results of (a) c-plane and (b) semipolar QW, respectively.

From the simulation result, it can be further clarified that the semipolar MQWs had smaller QCSE than the c-plane MQWs. And the internal electric field has been greatly suppressed on the semipolar surface, which alleviated the distortion of band diagram as well as the QCSE. Thus, the IQE can be improved.

4.3 Carrier dynamic of multiple quantum wells (MQWs)

Once the wave function overlap between electron and hole is enhanced, the transition probability of carriers in quantum well, which is associated with radiative recombination lifetime, is expected to be increased. . In this section, the radiative recombination lifetime was be qualitatively determined by time-resolved photoluminescence (TRPL).

4.3.1 Analysis of carrier lifetime

All experiment data were fitted by a combined exponential and stretched exponential line shape [56-58]:

$$I(t) = I_1(0) \exp\left(-\frac{t}{\tau_1}\right) + I_2(0) \exp\left(-\frac{t}{\tau_2}\right)^\beta \quad (4.3-1)$$

where $I(t)$ is the PL intensity at time t , β is the dimensionality of the localized centers [59-61], and τ_1 and τ_2 represent the initial lifetimes of the carriers. Normally, the fast decay term τ_1 is used represent τ_{PL} since the PL intensity is limited by the fast decay component [62].

The carrier lifetime in a semiconductor is related to nonradiative recombination centers, as illustrated in **Figure 4.3-1**. If the radiative lifetime is denoted as τ_r and the nonradiative lifetime is denoted as τ_{nr} , then the total probability of recombination is given by the sum of the radiative and nonradiative probability:

$$\frac{1}{\tau_{PL}} = \frac{1}{\tau_r} + \frac{1}{\tau_{nr}} \quad (4.3-1)$$

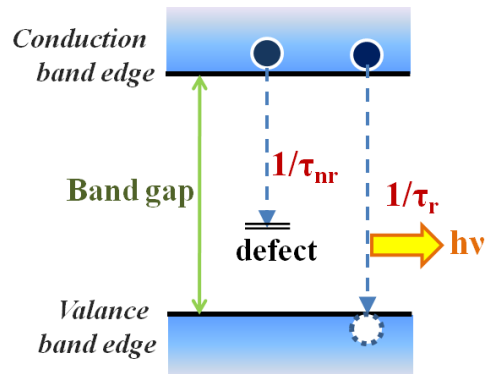


Figure 4.3-1 Illustration of radiative and nonradiative transition in a semiconductor.

The relative probability of radiative recombination is given by the radiative probability over the total probability of recombination. Therefore, the internal quantum efficiency (IQE) can be expressed in terms of the radiative and nonradiative lifetimes [63-64]:

$$\eta_{int} = \frac{\frac{1}{\tau_r}}{\frac{1}{\tau_r} + \frac{1}{\tau_{nr}}} = \frac{\tau_r^{-1}}{\tau_r^{-1} + \tau_{nr}^{-1}} \quad (4.3-2)$$

The IQE gives the ratio of the number of light quanta emitted inside the semiconductor to the number of charge quanta undergoing recombination. Note that not all photons emitted internally may escape from the semiconductor due to critical angle and reabsorption mechanisms.

By using the above equation, the internal quantum efficiency is determined by the competition between radiative and nonradiative recombination processes. In this material system, the radiative recombination rate is affected by the QCSE and exciton

localization effects.

At low temperature (regard as absolute 0 K), the carriers have no kinetic energy that the nonradiative probability is equal zero. The **Equation (4.3-1)** can be rewrite as

$$\tau_{PL} = \tau_r \quad (4.3-3)$$

However, as the temperature increases to room temperature (T=300 K), both of radiative and nonradiative processes have to be taken into account. To separate the τ_{PL} into τ_r and τ_{nr} , Using **Equation (4.2-2)** and **(4.3-2)** we can get the equation like this:

$$\tau_r = \frac{I_0}{I_{RT}} \tau_{PL} \quad (4.3-4)$$

And the τ_{nr} can be calculate from **Equation (4.3-1)**.

4.3.2 Experimental result and discussion

Figure 4.3-2 shown the TRPL spectrum of c-plane and semipolar MQWs at low temperature (LT) and room temperature (RT). From **Equation (4.3-1)**, the τ_{PL} can be calculated, as shown in **Figure 4.3-2**. It can be seen that the lifetime of the semipolar MQWs was faster than the c-plae MQWs at both of LT and RT, which means the carrier recombination probability of the semipolar MQWs was greater, that was consist with the results of IQE measurements.

Combining the results of IQE from PDPL measurements, we can calculate τ_r and τ_{nr} at room temperature from **Equation (4.3-4)**, as shown in the **Table 4.3-1**.

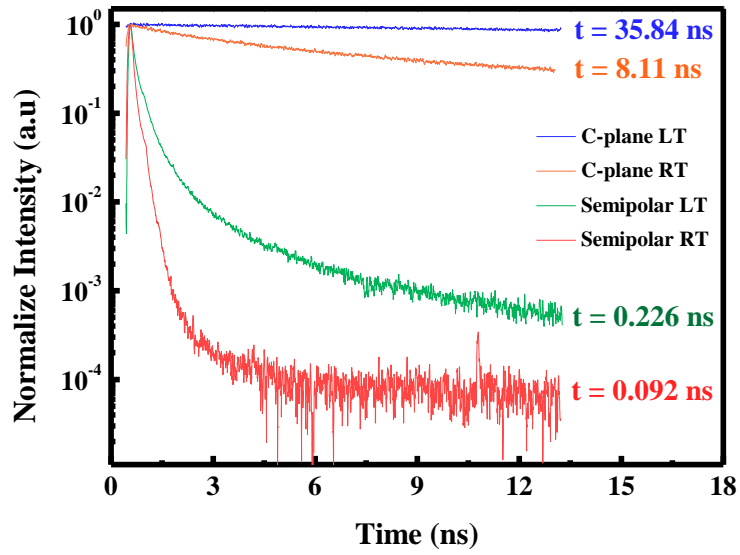


Figure 4.3-2 The TRPL spectrum of c-plane and semipolar MQWs at low temperature (LT) and room temperature (RT).

		C-plane	Semipolar
LT (15 K)	τ_r (ns)	35.84	0.22
RT (300 K)	I_0/I_{RT}	5.00	3.84
	τ_{PL} (ns)	8.11	0.09
	τ_r (ns)	40.55	0.34
	τ_{nr} (ns)	10.13	0.12

Table 4.3-1 The calculation result of τ_r and τ_{nr} from TRPL measurement.

Generally, τ_{nr} is smaller than τ_r at RT, as a result, the ratio of τ_r and τ_{nr} is very important. The smaller τ_r/τ_{nr} ratio means the higher radiative recombination property. The τ_r of the c-plane MQWs was about 4 times longer than the τ_{nr} . While for the semipolar MQWs, the magnitude was decrease to about 3 times. Therefore, the radiative process was more comparable with nonradiative process for semipolar MQWs.

From the optical experiment results, the semipolar MQWs can reduce the internal electron field (IEF) as well as the QCSE. Moreover, the wave function overlap between electron and hole can be enhanced, which increase the IQE and the radiative recombination time. These results were encouraging for developing high In composition green emitters by using semipolar {10-11} surface as a growth plane by SAE has great potential to solve the efficiency green gap of III-nitride light emitters.

Chapter 5. Electrical Property of III-nitride LED

In this section, we fabricated semipolar nanopyramid LED on GaN nanorod. The emission color of nanopyramid LED from olivine to orange were investigated. The following were the current-dependent electroluminescence (EL) spectrum behavior analysis of these samples.

5.1 Device performance of green nanopyramid LED

The background of **Figure 5.1-1** shows a photograph of green nanopyramid LED at a forward current of $I=50$ mA. A uniform emission distribution was observed over the entire chip area. The light output power density L (the solid dots) and the bias voltage V (the square dots) versus the forward current I of nanopyramid LED was shown in **Figure 5.1-1**. The electric properties were comparable with conventional c-plane LEDs [65]. Since the total active area of nanopyramid LED is estimated to be two times larger than planer c-plnae LED, the forward current should be doubled for comparing these two LED under the same current density. The output powers were measured with a calibrated integrating sphere. The light output power density of nanopyramid LED was 1500 mW/cm² at 40 mA [66-67]. The forward voltage (V_f) at 40 mA and series resistances (R_s) of nanopyramid LED are 3.61 V and 3.2Ω , respectively.

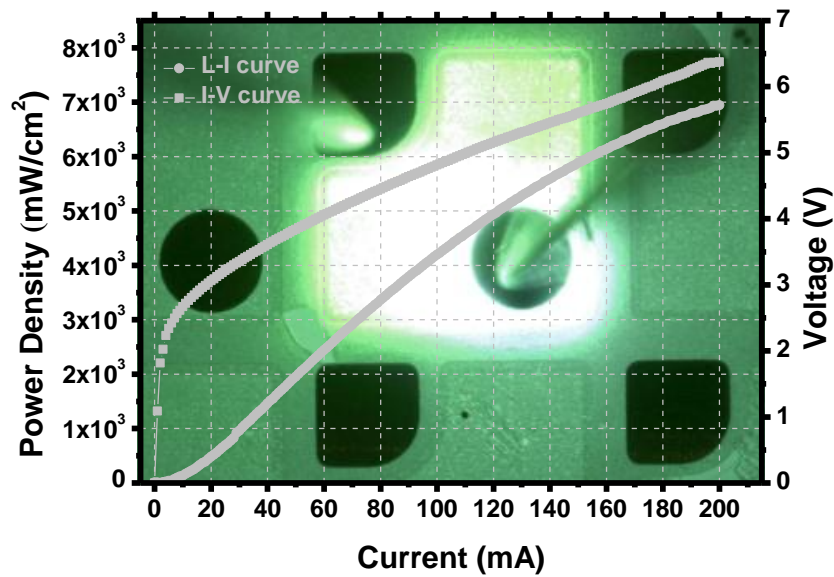


Figure 5.1-1 (Color online) The light output power density (mW/cm^2) versus forward current and current versus voltage of nanopyramid LED. Background: A photograph image taken under an injection current of 50 mA.

Figure 5.1-2 (a) shown the EL emission spectrum of nanopyramid LED with different injected current at room temperature. There were two emission peaks in the spectrum, the Peak 1 was about 500 nm and Peak 2 was about 560 nm under high injected current. From spatial resolved CL measurement result (**Figure 3.3-2 (d)** and **(g)**), the long wavelength at 560 nm was emitted from the apex of pyramids, and the short wavelength at 500 nm was emitted from the sidewall facets of pyramids.

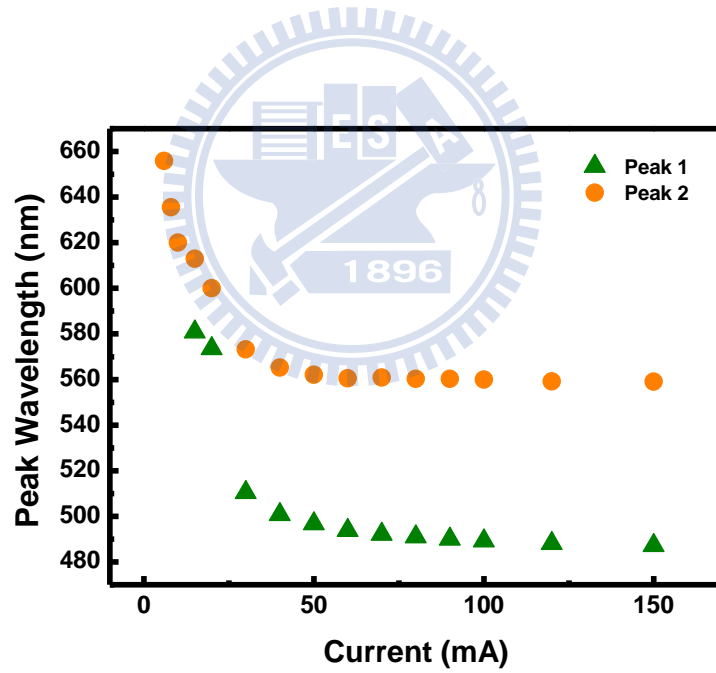
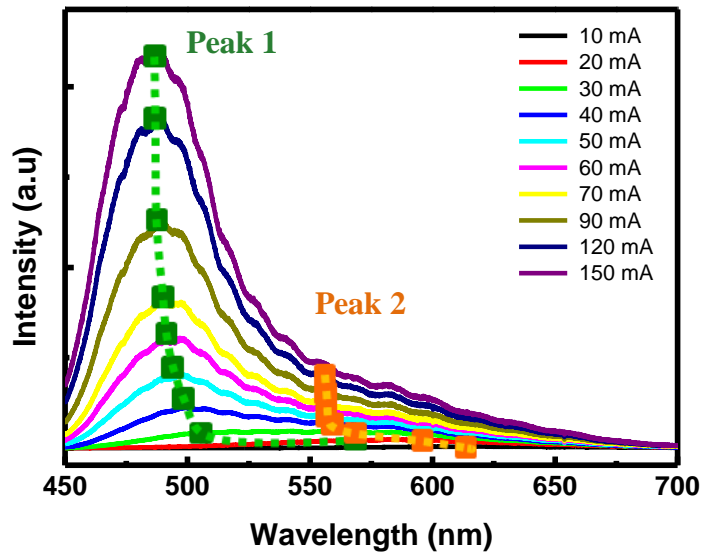


Figure 5.1-2 (a) The EL emission spectrum with different injected current at room temperature. (b) The two peaks wavelength shift from EL spectrum.

By analyzing the EL spectrum, the current-dependent peak shifts were derived and as shown in the **Figure 5.1-2 (b)**. There were two phenomenon in the figure can be observed. One was there existed only Peak 2 at very low current injection (<10 mA). Another was both peaks had strong blue shift in low injected current region, and become stable after 40 mA.

Red color emission can be observed at injection current was 10 mA, the corresponding emission wavelength was about 620 nm. Color change to olivine when increased the injection current to 30 mA, there were two dominate peaks can be observed, one was around 510 nm and 570 nm. After lager the injection current to 100 mA, the emission color changed from olivine to cyan, and the peak wavelength were 490 and 550 nm, respectively. EL luminescence images and the corresponding spectrum were shown in **Figure 5.1-3 (a)~(c)** and **Figure 5.1-4**. The dash lines were the result of Gauss multiple peaks fitting.

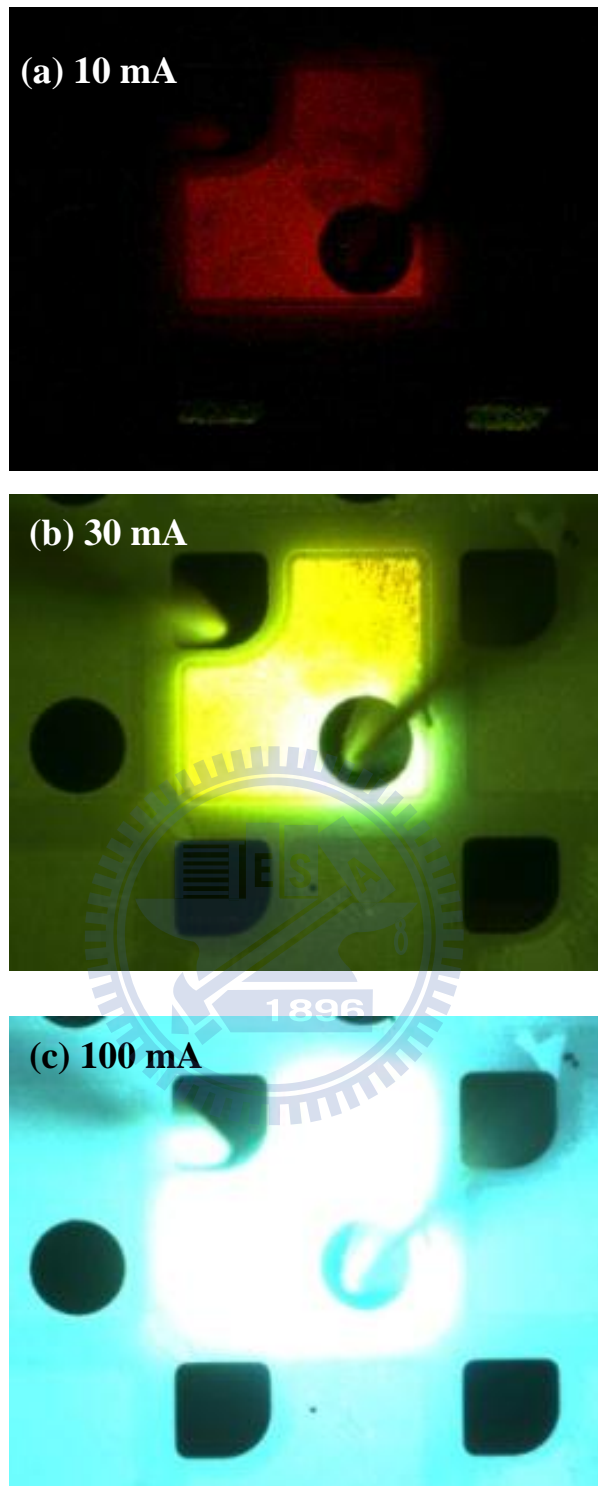


Figure 5.1-3 The photograph images taken under injection current of

(a) 10 mA, (b) 30 mA and (c) 100 mA.

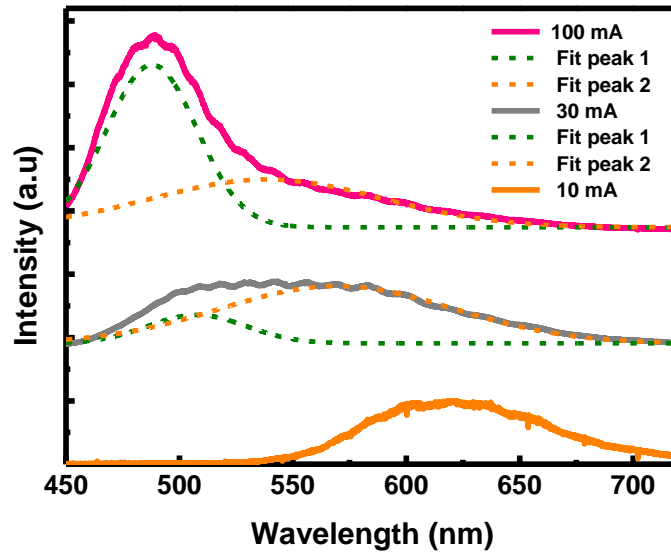


Figure 5.1-4 The EL spectrum under forward current of 10 mA, 30 mA and 100 mA, respectively (solid line). The results of Gauss multiple peaks fitting (Dash line).

From these results, we supposed a current injection model of the nanopyramid structure. By equation of charge density:

$$\rho = \frac{q}{4\pi r^2} \quad (5.2-1)$$

the smaller radius of curvature, the more current crowded. Therefore, from the measurement results by spatial resolved CL in **Figure 3.3-2**, the current was crowded at the apex of pyramids under very low current situation. Because of the current spreading layer (ITO), carriers injected into the pyramids uniformly when increase the injected current. Consequently, from **Figure 5.1-4**, the Peak 1 and Peak 2 ratio enlarged with injected current can be observed. These were the evidence of why only

Peak 1 can be observed under injected current lower than 10 mA and the main emission wavelength at 500 nm appeared in high injected current region. The schematic diagram of nanopyramid under different injected current was shown in

Figure 5.1-4.

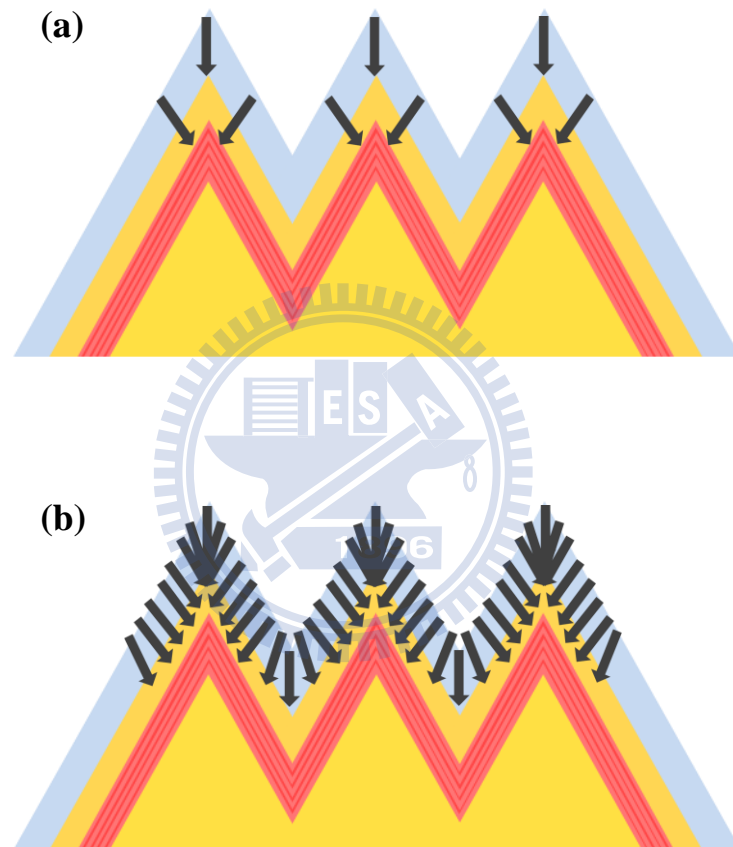


Figure 5.1-5 The schematic diagram of nanopyramid LED under (a) very low and (b) high injected current.

Moreover, **Figure 5.1-2** shown both peaks had strong blue shift in low injected current region, and saturate in high injected current region. The longer wavelength of both emission peaks at low injected current were emitted from localized states. And the significant blue shift was due to carrier filling in localized states. After filling of localized states, the peak emission wavelength was very stable which indicated the reduction of QCSE in semipolar MQWs. Worth a mention, the emission color would be very stable under normal operation current by using nanopyramid LED. The peak wavelength only made a 5 nm blue shift from 40 mA to 200 mA and stabilized at 495 nm, which evinced the low IEF properties of semipolar MQWs. Worthy of mention, the peak shift of conventional c-plane green LED was as large as 12 nm [68].

5.2 Device performance of olivine nanopyramid LED

As reducing 20°C ($T_g = 680^{\circ}\text{C}$) of growth temperature of MQWs, the emission color became olivine. The background of **Figure 5.2-1** shows a photograph of olivine nanopyramid LED at a forward current of 50 mA. The light output power density L (the solid dots) and the bias voltage V (the square dots) versus the forward bias current I of nanopyramid LED was shown in **Figure 5.2-1**. The light output power density of nanopyramid LED was 1300 mW/cm^2 at 40 mA. The forward voltage (V_f) at 40 mA and series resistances (R_s) of nanopyramid LED are 2.84 V and 3.5Ω , respectively.

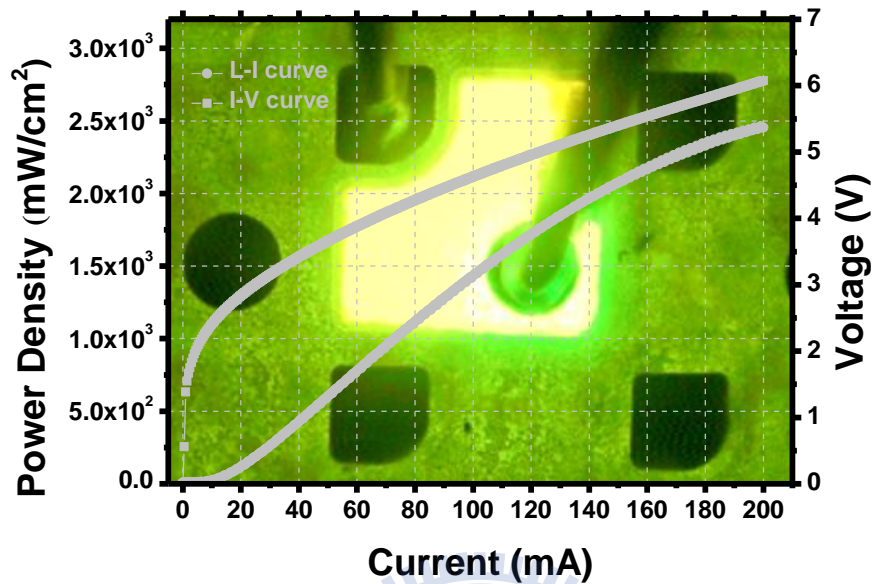


Figure 5.2-1 (Color online) The light output power density (mW/cm^2) and forward voltage versus forward current of nanopyr amid LED. Background: An electrical luminescence image taken under injection current 50 mA.

Figure 5.2-2 (a) shown the EL emission spectrum of nanopyr amid LED with different injected current at room temperature. There are two emission peaks in the spectrum, the Peak 1 and Peak 2 were 550 and 580 nm under high injected current. The localized state filling effect was dominated below 40mA, and emission peak became stable after 40 mA. The IEF could be remarkably suppressed at such long emission wavelength.

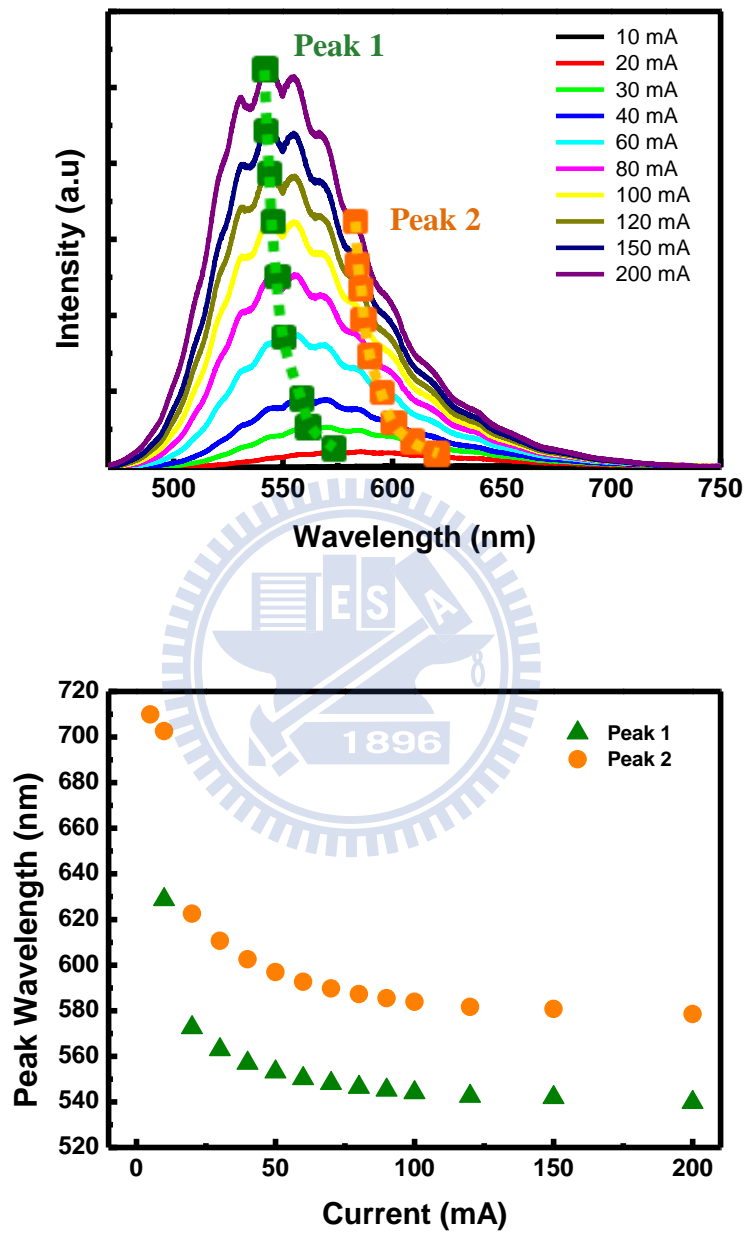


Figure 5.2-2 (a) The EL emission spectrum with different injected current at room temperature. (b) The peak wavelength shift from EL spectrum.

5.3 Device performance of orange nanopyramid LED

As further reduced the growth temperature of MQWs about 20°C ($T_g=660^\circ\text{C}$), the emission became orange color. The background of **Figure 5.3-1** shows a photograph of orange nanopyramid LED at a forward current of 200 mA. The light output power density of nanopyramid LED was 900 mW/cm² at 20 mA as shown in the **Figure 5.3-1**. The forward voltage (V_f) at 20 mA and series resistances (R_s) of nanopyramid LED are 2.22 V and 5.3 Ω , respectively.

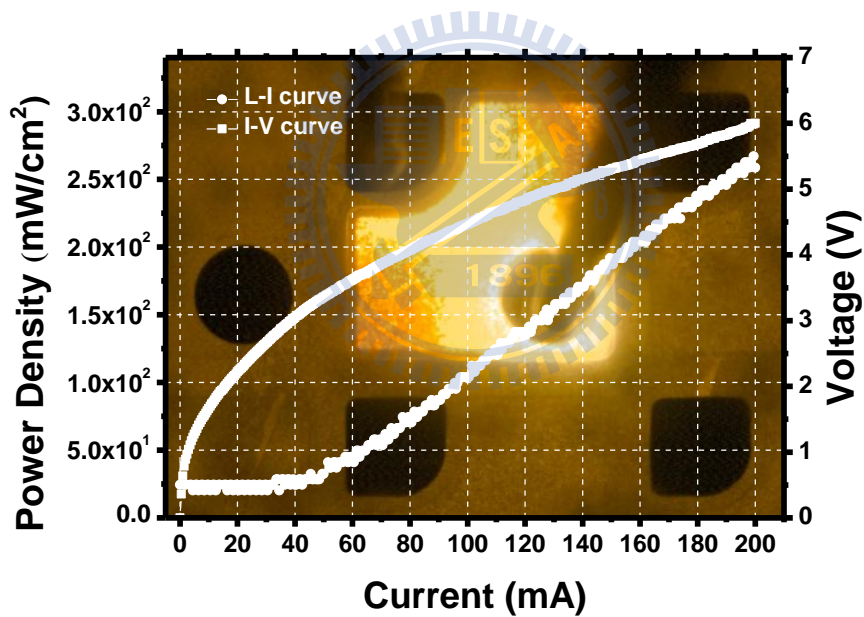


Figure 5.3-1 (Color online) The light output power density (mW/cm²) versus forward current and current versus voltage of nanopyramid LED. Background: A photograph image taken under an injection current of 200 mA.

Figure 5.3-2 (a) shown the EL emission spectrum with different injected current at room temperature. There are two emission peaks in the spectrum, the Peak 1 was about 600 nm and Peak 2 was about 640 nm under high injected current. The emission peaks of green, olivine and orange nanopyramid LEDs change with the same tendency comparing as increasing the forward current which evinced the QCSE could be greatly suppressed on semipolar surface at long emission wavelength region and the emission wavelength could even been pushed as long as 640 nm.



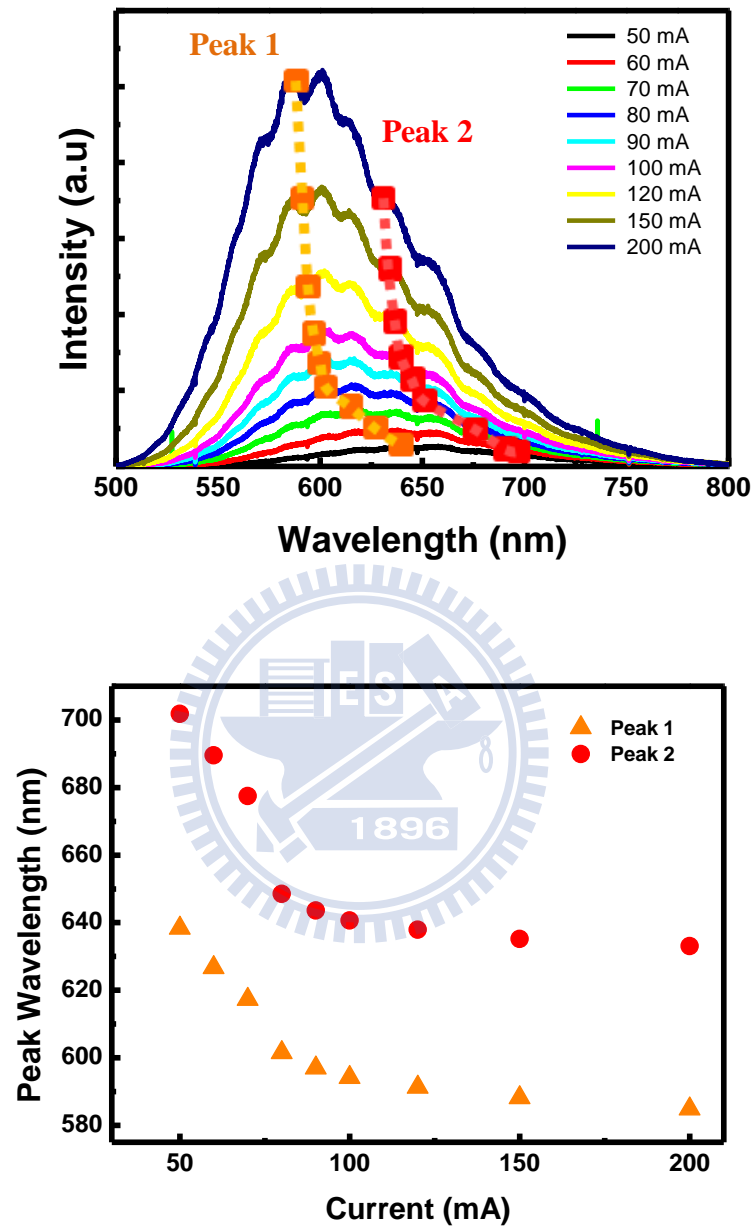


Figure 5.3-2 (a) The EL emission spectrum with different injected current at room temperature. (b) The peak wavelength shift from EL spectrum.

The characteristics of EL emission have been clearly described. From the EL measurement results, the nanopyramid LED with green, olivine and orange emission can be successful developed. Moreover, the nanopyramid structure had better In incorporation efficiency compared with c-plane. These results are encouraging to develop full color emitters by III-nitride {10-11} semipolar nanopyramid LEDs.



Chapter 6. Conclusion

In the first part, the fabrication of green emission semipolar {10-11} GaN-based LED on GaN nanopyramid template was given. The threading dislocation density (TDD) in semipolar MQWs was reduced through bending by epitaxy lateral overgrowth (ELO), which was shown in TEM images. The thickness of the quantum well and quantum barrier were uniform on the incline facet. Moreover, the longer emission signal was observed from the apex of pyramid by cathodoluminescence (CL) measurements, which shown that higher Indium content was formed by the geometrical structure and growth condition.

In the second part, we investigated the quality of semipolar {10-11} InGaN/GaN MQWs by photoluminescence measurements. Comparing with the c-plane MQWs, the internal electric field (IEF) of semipolar MQWs was drastically decreased from 1.7 MV/cm to 0.5 MV/cm. And the IQE enhancement was about 40% from c-plane to semipolar MQWs. From TRPL measurement, the radiative recombination lifetime of semipolar MQWs was shorter than that of c-plane MQWs. Moreover, semipolar MQWs had smaller ratio of τ_r/τ_{nr} at room temperature, which evince that radiative recombination process is more comparable with nonradiative process. These results can confirm the reduction of QSCE by using semipolar {10-11} MQWs.

In the third part, we used current dependent EL measurement to analysis the performances of green, olivine and amber emission nanopyramid LEDs. The *L-I-V*

curves and photograph images of emission were given. And the emission wavelength shift behavior was discussed. The light output power density of green nanopyramid LED is as high as 1500 mW/cm^2 at 40 mA and the electrical properties are comparable with conventional c-plane LEDs. It could be clearly seen that the peak wavelength only made a 5 nm blue shift from 40 mA to 200 mA and stabilized at 495 nm, which evinced the low IEF properties of semipolar MQWs. Besides, the light output power of olivine and orange LEDs were around 400 and 200 mW/cm^2 . The leakage became pronounced from green to orange emission, which resulted from poor crystalline quality as growing the orange emission MQWs at lowest temperature than others. It is worth noting that the emission peak can be pushed as long as 640 nm in the orange nanopyramid LED.

In summary, we successfully demonstrate the high quality green emission semipolar {10-11} GaN-based nanopyramid LED, which has great potential to develop high efficiency full color III-nitride light emitters.

Reference

- [1] S. Nakamura, M. Senoh, N. Isawa, and S. Nagahama, *Japan Journal of Applied Physics* 34, L797 (1995).
- [2] S. Nakamura, T. Mukai, and M. Senoh, *Applied Physics Letter* 64, 1687 (1994).
- [3] S. Nakamura, M. Senoh, S. Nagahama, N. Iwasa, T. Yamada, T. Matsushita, Y. Sugimoto, and H. Kiyoku, *Applied Physics Letter* 70, 868 (1997).
- [4] S. Nakamura, *Science* 281, 956 (1998).
- [5] Y. Arakawa, *IEEE Journal of Selected Topics in Quantum Electronics* 8, 823 (2002).
- [6] H. Morkoc, *Nitride Semiconductors and Devices* (Springer Verlag, Heidelberg), 1999.
- [7] S. N. Mohammad, and H. Morkoc, *Progress in Quantum Electronics* 20, 361 (1996).
- [8] F. Bernardini and V. Fiorentini, *Physica Status Solidi B* 216, 391 (1999).
- [9] A. Hangleiter, J. S. Im, H. Kollmer, S. Heppel, J. Off, and F. Scholz, *MRS Internet Journal of Nitride Semiconductor Research* 3, 15 (1998).
- [10] J. I. Pankove, E. A. Miller, and J. E. Berkeyheiser, *J. Luminescence*, 5, 84 (1992).
- [11] H. Amano, N. Sawaki, I. Akasaki, and Y. Toyoda, *Appl. Phys. Lett.*, 48, 353 (1986).
- [12] H. Amano, N. Sawaki, I. Akasaki, and Y. Toyoda, *Jpn. J. Appl. Phys.*, 28, L2112 (1989).
- [13] S. Nakamura, T. Mukai, M. Senoh, and N. Iwasa, *Jpn. J. Appl. Phys.*, 31, 1258 (1992).
- [14] S. Nakamura, T. Mukai, M. Senoh, S. Nagahama, and N. Iwasa, *Journal of Applied Physics*, 74, 3911 (1993).
- [15] Hisashi Masui and Shuji Nakamura, *IEEE Transactions on Electron Devices*, Vol. 57, NO. 1, (2010).

- [16] S. F. Chichibu, A. Uedono, T. Onuma, B. A. Haskell, A. Chakraborty, T. Koyama, P. T. Fini, S. Keller, S. P. DenBaars, J. S. Speck, U. K. Mishra, S. Nakamura, S. Yamaguchi, S. Kamiyama, H. Amano, I. Akasaki, J. Han, and T. Sota, *Nat. Mater.*, vol. 5, no. 10, pp. 810–816 (2006).
- [17] A. E. Romanov, T. J. Baker, S. Nakamura, and J. S. Speck, *J. Appl. Phys.*, vol. 100, no. 2, p. 023522 (2006).
- [18] H. Masui, S. Nakamura, S. P. DenBaars, and U. K. Mishra, *IEEE Trans. Electron Devices* vol. 57, pp. 88, (2010).
- [19] P. T. Barletta, E. A. Berkman, B. F. Moody, N. A. El-Masry, A. M. Emara, M. J. Reed, and S. M. Bedair, *Appl. Phys. Lett.* 90, 151109 (2007).
- [20] Y. J. Lee, S. Y. Lin, C. H. Chiu, T. C. Lu, H. C. Kuo, S. C. Wang, S. Chhajed, J. K. Kim, and E. F. Schurbert, *Appl. Phys. Lett.* 94, 141111 (2009).
- [21] J. Zhu, L. Wang, S. Zhang, H. Wang, D. Zhao, Zhu, Z. Liu, Jiang, and H. Yang, *J. Appl. Phys.* 108, 074302 (2010).
- [22] H.W. Lin, Y.J. Lu, H.Y. Chen, H.M. Lee, and S.J. Gwo, *Appl. Phys. Lett.* 97, 073101 (2010).
- [23] S. D. Hersee, X. Sun, and X. Wang, *Nano Lett.*, 6, 1808 (2006).
- [24] Y. L. Chang, J. L. Wang, F. Li and Z. Mi, *Appl. Phys. Lett.* 96, 013106 (2010).
- [25] H. Sekiguchi, K. Kishino, and A. Kikuchi, *Appl. Phys. Lett.* 96, 231104 (2010).
- [26] C. H. Chiu, M. H. Lo, T. C. Lu, P. Yu, H. W. Huang, H. C. Kuo, and S. C. Wang, *IEEE Journal of Lightwave Technology* 26, 1445 (2008).
- [27] W. Q. Han, S. S. Fan, Q. Q. Li, and Y. D. Hu, *Science* 277, 1287 (1997).
- [28] H. M. Kim, D. S. Kim, T. W. Kang, Y. H. Cho, and K. S. Chung, *Applied Physics Letter* 81 2193, (2002).
- [29] C. C. Yu, C. F. Chu, J. Y. Tsai, H. W. Huang, T. H. Hsueh, C. F. Lin, and S. C. Wang, *Japan Journal of Applied Physics* 41, L910 (2002).
- [30] W. Q. Han and A. Zettl, *Applied Physics Letter* 80, 303 (2002).
- [31] H. S. Chen, D. M. Yeh, Y. C. Lu, C. Y. Chen, C. F. Huang, T. Y. Tang, C. C. Yang, C.S.Wu, and C. D. Chen, *Nanotechnology* 17, 1454 (2006).
- [32] J. C. Johnson, H. J. Choi, K. P. Knutsen, R. D. Schaller, P. D. Yang, and R. J. Saykally, *Nature Material* 1 106 (2002).

- [33] S. Han, W. Jin, D. H. Zhang, T. Tang, C. Li, X. L. Liu, Z. Q. Liu, B. Lei, and C.W. Zhou, *Chemical Physics Letter* 389, 176 (2004).
- [34] H. M. Kim, Y. H. Cho, H. Lee, S. I. Kim, S. R. Ryu, D. Y. Kim, T.W. Kang and K. S. Chung, *Nano Letter* 4 1059 (2004).
- [35] M. S. Son, S. I. Im, Y. S. Park, C. M. Park, T.W. Kang, and K. H. Yoo, *Material Science and Engineering C-Biomimetic and Supramolecular System* 26, 886 (2006).
- [36] W Bergbauer, M Strassburg, Ch Kolper, N Linder, C Roder, J Lahnemann, A Trampert, S Fundling, S F Li, H-H Wehmann and A Waag, *Nanotechnology*, 21, 305201 (2010).
- [37] I. H. Wildeson, R. Colby, D. A. Ewoldt, Z. Liang, D. N. Zakharov, N. J. Zaluzec, R. E. Garcia, E. A. Stach, and T. D. Sands, *J. Appl. Phys.* 108, 044303 (2010).
- [38] G. T. Chen, S. P. Chang, J. I. Chyi and M. N. CHangi, *Appl. Phys. Lett.*, 92, 241904 (2008).
- [39] Yi-Chen Chen, Kuok-Pan Sou, Shih-Pang Chang, Ji-Kai Huang, Da-Wei Lin, Ching-Hsueh Chiu, Zhen-Yu Li, Chi-Wai Chow, and Hao-Chung Kuo, *International Conference on Optics and Photonics Taiwan* (2010).
- [40] Wolfgang Becker, the bh TCSPC Handbook (2006).
- [41] Wolfgang Becker, *Advanced time-correlated single-photon counting techniques*. Springer, Berlin, Heidelberg, New York, (2005).
- [42] D.V. O' Connor, D. Phillips, *Time-correlated single photon counting*, Academic Press, London (1984).
- [43] Yguerabide, *Nanosecond fluorescence spectroscopy of macromolecules*, *Meth. Enzymol.* 26, 498-578 (1972).
- [44] P. Frajtag, A. M. Hosalli, G. K. Bradshaw, N. Nepal, N. A. El-Masry, and S. M. Bedair, *Appl. Phys. Lett.* 98, 143104 (2011).
- [45] H. Fang, Z. J. Yang, Y. Wang, T. Dai, L. W. Sang, L. B. Zhao, T. J. Yu, and G. Y. Zhang, *J. Appl. Phys.* 103, 014908 (2008).
- [46] P. L. Bonanno, S. M. O'Malley, A. A. Sirenko, A. Kazimirov, Z.-H. Cai, T. Wunderer, P. Brückner, and F. Scholz, *Appl. Phys. Lett.* 92, 123106 (2008).
- [47] A. Chtanov, T. Baars, and M. Gal, *Phys. Rev. B*, vol. 53, 4704 (1996).

- [48] C. Y. Lai, T. M. Hsu, W.-H. Chang, and K.-U. Tseng, C.-M. Lee, C.-C. Chuo, and J.-I. Chyi, *J. Appl. Phys.*, vol. 91, 531 (2002).
- [49] Guan-Ting Chen, Shih-Pang Chang, Jen-Inn Chyi, and Mao-Nan Chang, *Appl. Phys. Lett.*, 92, 241904 (1962).
- [50] T. Kanata, M. Matsunaga, H. Takakura, Y. Hamakawa, and T. Nishino, *Proc. SPIE* 56, 1286 (1990).
- [51] See, for example, S. M. Sze, *Physics of Semiconductor Devices*, 2nd ed. (Wiley, New York, 1981), p. 794.
- [52] X. Yin, H. M. Chen, F. H. Pollak, Y. Cao, P. A. Montano, P. D. Kirchner, G. D. Pettit, and J. M. Woodall, *J. Vac. Sci. Technol. A* 10, 131 (1992).
- [53] J. I. Pankove, *Optical Processes in Semiconductors* (Dover, New York, 1971), p. 27.
- [54] I. V. Rozhansky and D. A. Zakheim, *Phys. Status Solidi A* 204, 227 (2007)
- [55] M. H. Kim, M. F. Schubert, Q. Dai, J. K. Kim, E. F. Schubert, J. Piprek, and Y. F. Bernardini, V. Fiorentini, and D. Vanderbilt, *Phys. Rev. B* 56, R10024 (1997)
- [56] S. F. Chichibu, T. Onuma, T. Aoyama, K. Nakajima, P. Ahmet, T. Chikyow, T. Sota, S. P. DenBaars, S. Nakamura, T. Kitamura, Y. Ishida, and H. Okumura, *J. Vac. Sci. Technol. B*, Vol. 21, No. 4, (2003)
- [57] Ralf Metzler, Joseph Klafter, *Journal of Non-Crystalline Solids* 305 (2002)
- [58] Thomas Wunderer, a Peter Brückner, Joachim Hertkorn, Ferdinand Scholz, Gareth J. Beirne, Michael Jetter, Peter Michler, Martin Feneberg and Klaus Thonke, *Appl. Phys. Lett.* 90, 171123 (2007).
- [59] M. Zhang, J. Moore, Z. Mi, P. Bhattacharya, *Journal of Crystal Growth* 311 (2009) 2069–2072.
- [60] Y. J. Sun, O. Brandt, S. Cronenberg, S. Dhar, H. Grahn, K. Ploog, P. Waltereit, and J. S. Speck, *Phys. Rev. B* 67, 041306 R (2003).
- [61] T. Onuma, A. Chakraborty, B. A. Haskell, S. Keller, S. P. DenBaars, J. S. Speck, S. Nakamura, and U. K. Mishra, *Appl. Phys. Lett.*, 86, 151918 (2005).
- [62] Ralf Metzler and Joseph Klafter, *Journal of Non-Crystalline Solids* 305 (2002) 81-87.

- [63] T. Li, A. M. Fischer, Q. Y. Wei, F. A. Ponce, T. Detchprohm, and C. Wetzel, *Appl. Phys. Lett.*, 96, 031906 (2010).
- [64] Y. Narukawa, S. Saijou, Y. Kawakami, S. Fujita, T. Mukai, and S. Nakamura, *Appl. Phys. Lett.*, 74, 558 (1999).
- [65] C. H. Wang, C. C. Ke, C. Y. Lee, S. P. Chang, W. T. Chang, J. C. Li, Z. Y. Li, H. C. Yang, H. C. Kuo, T. C. Lu and S. C. Wang, *Appl. Phys. Lett.* 97, 261103 (2010).
- [66] Ya-Ju Lee, Shawn-Yu Lin, Ching-Hua Chiu, Tien-Chang Lu, Hao-Chung Kuo, Shing-Chung Wang, Sameer Chhajed, Jong Kyu Kim, and E. Fred Schubert, *Appl. Phys. Lett.* 94, 141111 (2009).
- [67] Liang-Yi Chen, Ying-Yuan Huang¹, Chun-Hsiang Chang, Yu-Hsuan Sun, Yun-Wei Cheng, Min-Yung Ke, Cheng-Pin Chen and JianJang Huang, *Opt. Express* 18, 7664 (2010).
- [68] R. Sharma, P. M. Pattison, H. Masui, R. M. Farrell, T. J. Baker, B. A. Haskell, F. Wu, S. P. DenBaars, J. S. Speck, and S. Nakamura, *Appl. Phys. Lett.* 87, 231110 (2005).

